The Heat Budget of a Midlatitude Squall Line and Implications for Potential Vorticity Production

SCOTT A. BRAUN AND ROBERT A. HOUZE JR.

Department of Atmospheric Sciences, University of Washington, Seattle, Washington

(Manuscript received 7 December 1994, in final form 1 August 1995)

ABSTRACT

The water and heat budgets for a midlatitude squall line are estimated from single- and dual-Doppler-radar data and thermodynamic data from rawinsonde and thermodynamic retrieval (from dual-Doppler winds). These data, along with models to retrieve the freezing, melting, and radiative heating rates, yield vertical profiles of the heating within the convective, stratiform, and overhanging anvil areas of the squall line and differentiate the processes contributing to the total heating. The use of radar-derived vertical velocity information provides a more accurate delineation of the convective and stratiform components of the heating than can be obtained from rawinsonde data.

The effects of diabatic heating on the potential vorticity (PV) field are calculated using a simple two-dimensional model and the vertical profiles of heating from the heat budget. The diabatic heating produced a deep column of high PV air coincident with the convective region and produced several regions of negative PV. Similar regions of negative PV were observed in the squall line. Upper-level negative PV within and to the rear of the stratiform precipitation region suggests that symmetric or inertial instability might favor intensification of the upper-level line-normal outflow there. Anticyclonic inertial turning of this outflow contributes to the formation of a strong upper-level jet in the line-parallel flow to the rear of the squall line.

1. Introduction

Midlatitude mesoscale convective systems (MCSs) can produce and modify mesoscale and synoptic-scale weather systems. In baroclinic environments, deep convection can enhance or modify the development of synoptic-scale cyclonic storms. For example, in the strong baroclinity of explosive cyclones, diabatic heating often enhances development of the cyclone, though it does not change the basic processes or dynamics of the cyclogenesis (Davis et al. 1993). In weaker baroclinic environments, such as often prevail over the central United States during summer months, diabatic heating may provide more significant forcing of cyclogenesis relative to dry baroclinic processes (Zhang and Harvey 1995). In very weak baroclinic environments, heating by MCSs can generate mesoscale vortices (Bartels and Maddox 1991; Johnson and Bartels 1992), some of which can subsequently trigger new convection and produce very long lived mesoscale convective systems (Bosart and Sanders 1981; Zhang and Fritsch 1987, 1988; Chen and Frank 1993; Fritsch et al. 1994).

In this study, we examine a midlatitude squall line that occurred in a moderate baroclinic environment and contributed to the development of a weak cyclone. This squall line and the subsequent cyclone formed in the lee of the Rocky Mountains on 10–11 June 1985 during the Oklahoma–Kansas Preliminary Regional Experiment for the Stormscale Operational and Research Meteorology Program-Central Phase (PRE-STORM; Cunning 1986). Many investigators have studied this storm (e.g., Augustine and Zipser 1987; Smull and Houze 1987; Johnson and Hamilton 1988; Rutledge et al. 1988; Zhang et al. 1989; Biggerstaff and Houze 1991a, 1991b, 1993; Zhang 1992; Braun and Houze 1994, 1995b; Zhang and Harvey 1995). Cyclogenesis began during the later stages of the squall line and continued after its dissipation. Zhang and Harvey (1995) described the evolution of the surface cyclone and the contribution of the squall line to the cyclogenesis. They concluded that the squall line, particularly its associated diabatic heating, produced a more favorable westward phase-tilt of the baroclinic wave, thereby substantially modifying the cyclone development.

Since the heating associated with the squall line contributed significantly to the cyclogenesis, we document the interaction of the MCS and the larger-scale flow via a large-scale budget of heating. A water budget is also derived in order to obtain the heat budget. Such studies are frequently performed with data collected at scales comparable to, or somewhat larger than, the convective systems. For example, Gallus and Johnson (1991, hereafter GJ) constructed a heat budget of the 10–11 June

Corresponding author address: Mr. Scott A. Braun, National Center for Atmospheric Research, P.O. Box 3000, Boulder, CO 80307-3000.

© 1996 American Meteorological Society

squall line from composites of rawinsonde data from National Weather Service and PRE-STORM supplemental sites. They interpolated composite data to grids of spacing 0.5° in latitude and longitude. This resolution made it difficult for them to delineate precisely the convective and stratiform precipitation region contributions to the heat budget since their composite analysis aliased convective-region vertical velocities into the trailing stratiform precipitation region.

Our objective is to obtain a more complete and precise analysis of all the processes contributing to the heat budget than can be obtained from soundings alone and to resolve the processes occurring on a wider range of scales within the storm. As part of this effort, we calculate the heat and water budgets of the 10–11 June squall line from dual-Doppler-radar data (sections 5–6). The budgets resolve the separate processes occurring in the convective and stratiform precipitation regions of the storm. Radiative heating within nonprecipitating anvil[1] regions (referred to as anvil hereafter) are also estimated. Although this analysis examines only a small portion of the mesoscale convective system, it resolves the heating down to the scale of the convective motions so that contributions from different regions of the storm (convective, stratiform, anvil) are delineated.

Cyclone development has been increasingly discussed in terms of potential vorticity anomalies, their associated wind and thermodynamic fields (obtained through inversion techniques), and their mutual interactions (Hoskins et al. 1985; Davis et al. 1993). Hertenstein and Schubert (1991, hereafter HS91) discussed the production of potential vorticity anomalies by the heating associated with deep convection and accompanying stratiform precipitation regions. A further objective of our study is to expand upon the results of HS91 by calculating the potential vorticity effects of squall-line heating based on the magnitude and vertical distribution of heating from the heat budget (section 7).

2. Formulation of the water and heat budgets

Water budgets of leading line–trailing stratiform squall lines are typically divided into their convective and stratiform precipitation region components. The water budget equations are expressed as follows.

In the convective region,

$$R_c = C_{cu} - E_{cd} - C_{af} - C_a - S_c, \qquad (1)$$

where R_c is the convective rainfall, C_{cu} is the total condensate produced in convective updrafts, E_{cd} is the total condensate evaporated in convective downdrafts, C_{af} is the condensate transported into the forward anvil overhang (and eventually evaporated into the environment ahead of the line), C_a is the condensate transported rearward into the stratiform region, and S_c is the storage in the convective region.

In the stratiform region, the water budget equation is

$$R_s = C_a + C_{su} - E_{sd} - C_{ar} - S_s, \qquad (2)$$

where R_s is the stratiform rainfall, C_{su} is the total condensate produced in the mesoscale updraft, E_{sd} is the condensate evaporated in the mesoscale downdraft, C_{ar} is the condensate transported into the rear anvil overhang (which is eventually evaporated into the environment to the rear of the system), and S_s is the storage of condensate in the stratiform region.

The convective and stratiform rainfall are determined from raingauge observations from the PRE-STORM mesonetwork of surface stations (section 3b). The total condensate produced and evaporated in updrafts and downdrafts, respectively, are estimated in a manner similar to the heat budget (section 4a). The remaining terms in the water budget are derived according to assumptions about the mass of condensate transferred into the forward and rear anvil clouds and the storage of condensate in the convective and stratiform regions (section 5).

We estimate the heating by microphysical and radiative processes for the 10–11 June squall line and formulate the budget following Houze (1982). The heat budget of a large-scale area A containing the mesoscale convective system is obtained from an equation for the conservation of dry static energy $s = c_pT + gz$, where T is temperature, c_p is the specific heat of air at constant pressure, g is the gravitational acceleration, and z is height. The heating within the large-scale area A is

$$\frac{\partial \overline{s}}{\partial t} + \frac{1}{A}\oint V_n s\,dl + \frac{1}{\rho}\frac{\partial}{\partial z}(\rho \overline{ws}) - \sigma_e Q_{re}$$
$$= \sigma_{cl} Q_{rcl} + L_v(\overline{c} - \overline{e}) + L_s(\overline{\mathfrak{d}} - \overline{\mathfrak{s}}) + L_f(\overline{\mathfrak{f}} - \overline{\mathfrak{m}})$$
$$- \frac{1}{\rho}\frac{\partial}{\partial z}[\rho \sigma_{cl}(1 - \sigma_{cl}) w_{cl}(s_{cl} - s_e)], \qquad (3)$$

where V_n is the component of the horizontal velocity normal to the boundary of A; dl is an element of length along the boundary; w is the vertical velocity; ρ is the density of air; Q_{re} and Q_{rcl} are the radiative heating rates in the cloud-free and cloudy areas; $\mathfrak{c}$, $\mathfrak{e}$, $\mathfrak{d}$, $\mathfrak{s}$, $\mathfrak{f}$, and $\mathfrak{m}$ are the heating rates associated with condensation, evaporation, deposition, sublimation, freezing, and melting; and L_v, L_s, and L_f are the latent heats of vaporization, sublimation, and fusion, respectively. Term σ_{cl} is the fraction of A covered by clouds and can be subdivided into convective, stratiform, and anvil components (σ_c, σ_s, and σ_a), and σ_e is the fraction of A not covered by clouds. The last term on the right side of (3) is the convergence of the vertical eddy flux of sen-

[1] In this paper, the term anvil is used to describe stratiform cloud areas *lacking* surface precipitation, while the term stratiform region refers to stratiform cloud regions *producing* surface precipitation.

sible heat. The mean environmental vertical motion has been neglected in this term. The horizontal eddy heat flux convergence is contained within the integral on the left side of (3).

This study uses a method similar to Houze (1982), except that observations of the 10–11 June storm are used in place of the idealized characteristics assumed in that study. Water and heat budgets are estimated for two periods of the squall line's life cycle. The first period is the early stage of the squall line (~0030–0230 UTC), during which time the stratiform precipitation region was weak and accounted for only 10%–20% of the total precipitation. The second period covers the mature stage of the squall line (~0330–0530 UTC), in which nearly 30%–40% of the precipitation was stratiform.

3. Data and characteristics of the 10–11 June squall line

a. Area definitions

The heat budget is calculated for an area $A = 700 \times 700$ km^2, enclosing the approximately 650 km long squall line. Figure 1 shows the approximate boundary of the cloud shield of the 10–11 June squall line estimated from satellite data within the 700×700 km^2 area at 0151 UTC (Fig. 1a) and 0351 UTC (Fig. 1b) 11 June. The total cloud area increased from covering 61% of the large-scale area (area of the figure panel) at 0151 UTC to 73% of the area at 0351 UTC. After this time, the horizontal extent of the cloud shield remained relatively steady for several hours.

Approximate areas for the precipitation regions (convective and stratiform) were estimated from low-level PPI scans from the NWS WSR-57 radars at Wichita, Kansas, Oklahoma City, Oklahoma, and Amarillo, Texas. The proximate areas of the convective and stratiform precipitation regions are indicated by the shading (not actual reflectivities) in Fig. 1. At both times, the convective region was approximately 35 km wide and 650 km long. At 0151 UTC, the stratiform region was relatively narrow and weak, extending in the across-line direction approximately 85 km and in the along-line direction about 600 km. At 0351 UTC, data from the Amarillo radar were unavailable. Based on the data available at this time and that at subsequent times (see Fig. 13d of Johnson and Hamilton 1988), the stratiform region width was 120 km and its length was approximately the same as the convective line (~650 km). These dimensions and the total cloud areas determined from satellite partition the total cloud area A_{cl} into its convective, stratiform, and anvil components A_c, A_s, and A_a (Table 1).

b. Rainfall

Rainfall rates and accumulations for the water budget were determined from the surface network of 42 NCAR Portable Automated Mesonetwork (PAM)

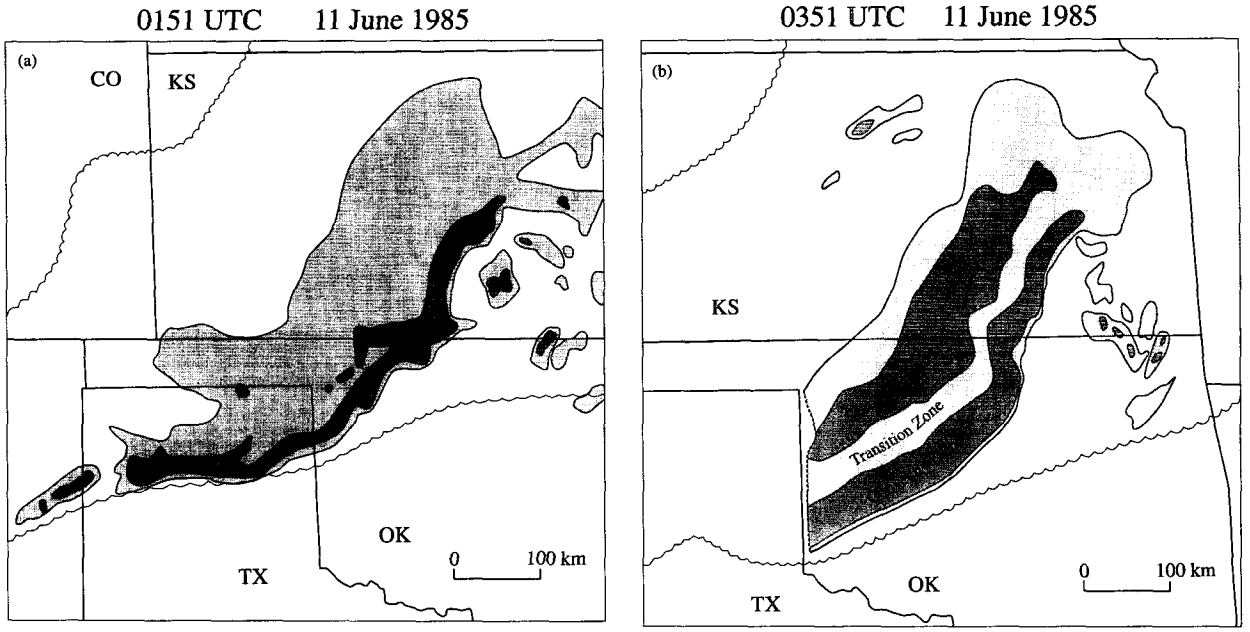

FIG. 1. Cloud outline (scalloped line) and precipitation regions (shaded) at (a) 0151 UTC and (b) 0351 UTC 11 June 1985. In (a), the convective line and isolated convective cells are indicated by the dark shading. Stratiform precipitation and weaker convective echoes are indicated by the light shading. In (b), the shading convection is the same except that the secondary maximum of reflectivity (or secondary band) in the stratiform region is highlighted by dark shading. Data from the Amarillo, Texas, radar were missing at 0351 UTC.

TABLE 1. Areal coverages and fractional areas of the convective, stratiform, overhanging anvil, and total cloud regions.

	Time	Convective	Stratiform	Anvil	Total cloud
Area (km^2)	0151	2.3×10^4	5.1×10^4	2.3×10^5	3.0×10^5
Area (km^2)	0351	2.3×10^4	7.8×10^4	2.6×10^5	3.6×10^5
Fractional area	0151	0.05	0.10	0.47	0.61
Fractional area	0351	0.05	0.16	0.53	0.73

and 42 NSSL Surface Automated Mesonetwork (SAM) stations for the period 0000–0800 UTC 11 June 1985. Thirteen stations in each group were found to have suspect or missing data and were excluded from the analysis. The rainfall was separated into convective and stratiform components following Johnson and Hamilton (1988). The convective rainfall was assumed to begin with the first nonzero 5-min rainfall rate occurring at the leading edge of the convective rainfall spike. The rear of the convective rainfall was assumed to be where the rainfall rate fell below 6 mm h^{-1}. All rainfall occurring after this time was considered to be stratiform even if the rainfall rate exceeded 6 mm h^{-1} at a later time.

The total convective and stratiform rainfall for each station was determined by summing over the 8-h period. The total convective and stratiform rainfall for each 5-min period between 0000–0800 UTC was determined by summing over all stations. Figure 2 shows time series of the total rainfall amounts for the convective and stratiform regions and the fraction of the total rainfall produced within the stratiform precipitation region. During the early stages of the storm (0030–0230 UTC), the stratiform rainfall accounted for only about 5%–20% of the total rainfall measured by the raingauge network. After 0330 UTC, the stratiform rainfall increased while the rainfall associated with the weakening convective line tended to decrease. Between 0400 and 0600 UTC, the stratiform rainfall accounted for approximately 35%–45% of the total rainfall. After 0600 UTC, the stratiform rainfall fraction increased from 40% to near 100% as the convective line diminished and moved out of the network of surface stations.

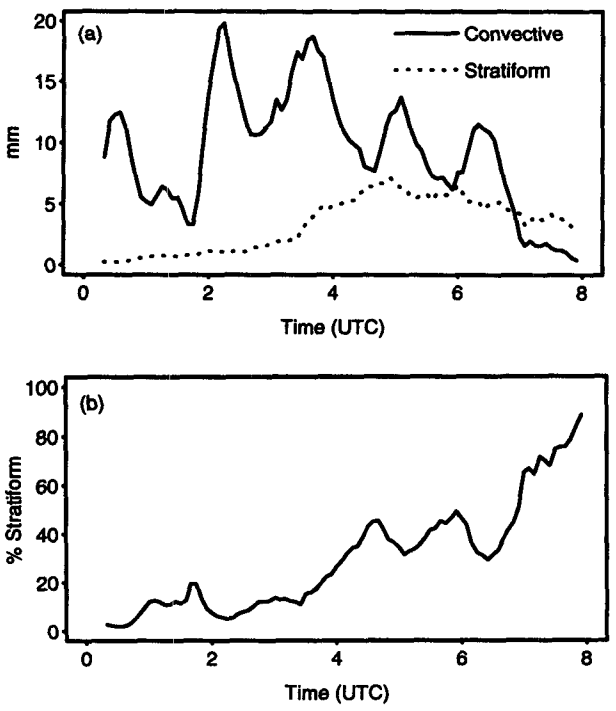

FIG. 2. Time series of (a) area-integrated convective (solid) and stratiform (dotted) rainfall amount and (b) the stratiform contribution (percent of total) to the total rainfall determined from raingauge data.

The total convective and stratiform rainfall measured by the raingauges for the 8-h period were 873 and 317 mm, respectively (Table 2). Therefore, the stratiform rainfall accounted for approximately 27% of the total rainfall measured by raingauge during this period, consistent with the results of Johnson and Hamilton (1988). The average convective and stratiform rainfall rates for the 8-h period were 20.9 and 2.9 mm h^{-1}, respectively. Average rainfall rates were also determined for the periods considered in the water budgets. For the early stage (0030–0230 UTC), the average convective and stratiform rainfall rates were 21.2 and 2.0 mm h^{-1}. For the mature stage (0330–0530 UTC), the average rates were 22.2 and 3.2 mm h^{-1}.

c. *Vertical velocities*

Three volumes of dual-Doppler synthesized winds and reflectivity characterize the convective vertical motions during the early stage: the west[2] dual-Doppler lobe at 0131 UTC and the east dual-Doppler lobe at 0139 and 0209 UTC 11 June. Low-level reflectivities for these times are shown in Fig. 3. Averaging the vertical velocities within the polygons yielded profiles of mean updraft velocity and mean downdraft velocity (Fig. 4) for each volume. The mean vertical velocities (not shown) within the polygons for each dual-Doppler volume are simply the sum of the updraft and downdraft components. Heating rates are calculated for each

[2] See Biggerstaff and Houze (1991a) for a description of the west and east dual-Doppler lobes.

set of updraft and downdraft profiles and then averaged to obtain mean heating rates for the convective region.

The updraft profiles in Fig. 4 are similar above 3 km, with peak mean velocities of about 2.2 m s^{-1}. The downdraft profiles vary considerably. The downdrafts at 0209 UTC were weaker throughout the troposphere than at 0131 and 0139 UTC. At 0131 UTC, two distinct peaks in downward motion are evident. The low-level peak was associated with downdrafts driven by precipitation loading and evaporation. Biggerstaff and Houze (1993), Yang and Houze (1995a), and Yuter and Houze (1995) have provided evidence that the upper-level peak in downward motion was associated with gravity waves.

No dual-Doppler observations of the convective region are available during the mature stage since the line had moved out of the dual-Doppler domain. As a result, we must make assumptions regarding the vertical motions, and hence heating, within the convective region during this period. We assume that the shape of the mean convective heating profile is unchanged; however, the magnitudes of the heating rates are scaled according to water budget constraints discussed in section 5. Consequently, convective-region budget calculations for the mature stage are limited by this assumption.

For the stratiform region during the early stage, we use the EVAD[3]-derived time-mean vertical motions of Rutledge et al. (1988, their Fig. 15) for the CP-3 radar. We use the EVAD profile since the vertical velocity estimates from the EVAD analysis are expected to be more accurate than the dual-Doppler synthesized motions within the stratiform region. Low-level radar reflectivity plots in Rutledge et al. (1988) indicate that CP-3 profiles at individual times were first obtained before the secondary maximum of reflectivity[4] formed in the stratiform region (<0300 UTC) and then later near the rear edge of the stratiform region (to the rear of the secondary maximum of radar reflectivity, ~0345 UTC). The vertical velocity profile (Fig. 5, solid line) shows strong and deep mesoscale descent below about 6 km with ascent above this level. Since the 0°C level was located near 4 km, the descent between 4 and 6 km suggests that sublimation cooling contributed to the initiation of mesoscale descent (Stensrud et al. 1991). This sublimation was occurring within the dry rear-inflow current that extended across the stratiform precipitation region (see Figs. 7 and 9a of Rutledge et al. 1988).

To verify that the CP-3 vertical motion profile is representative of the stratiform region at early stages, we have averaged the dual-Doppler vertical motions in the area behind the convective line at 0131 UTC (dotted polygon in Fig. 3a). This vertical motion profile is also shown in Fig. 5 (dot-dashed line). The 0131 UTC and CP-3 profiles are very similar, justifying our use of the CP-3 profile to estimate the stratiform region heating rates during the early stages of the squall line.

TABLE 2. Rainfall characteristics of the 10-11 June squall line. The 8-h period covers 0000 to 0800 UTC 11 June. The early stage covers the period from 0030 to 0230 UTC and the mature stage from 0330 to 0530 UTC.

	Convective	Stratiform
8-h Total rainfall (mm)	873	317
8-h Average rainfall rate (mm h^{-1})	20.9	2.9
Average rainfall rate, early stage	21.2	2.0
Average rainfall rate, mature stage	22.2	3.2

For the stratiform region during the mature stage, we use the EVAD-derived time-mean vertical velocities of Rutledge et al. (1988) for both the CP-3 and CP-4 radars. The CP-4 vertical velocity profile (Fig. 5, dotted line), characteristic of the secondary maximum region in the stratiform region, shows significant differences from the CP-3 profile. It is characterized by deeper and stronger ascent associated with a deeper stratiform cloud layer. The more moist conditions in this region above 0°C (see section 3d, Fig. 7b) suggest that sublimation cooling had much less influence so that the top of the descent was lowered to near the melting level. The deeper descent layer in the CP-3 profile, taken near the rear of the stratiform precipitation region, is indicative of the slope of the descent (and rear inflow) across the stratiform region (see Figs. 5–7, 13, and 14 of Rutledge et al. 1988).

The CP-3 vertical motions during this period were characteristic of that portion of the stratiform region to the rear of the secondary band, which accounted for approximately 20% of the stratiform area. In contrast, the CP-4 vertical velocities were typical of the mature secondary band (high reflectivity area) in the stratiform region, which accounted for about 80% of the stratiform area. This partitioning of the stratiform precipitation region was based on vertical reflectivity structures shown in Figs. 5–7 of Rutledge et al. (1988). The water and heat budget results for the mature-stage stratiform region are obtained from an area-weighted average of the water and heat budgets calculated from the CP-3 and CP-4 velocity data. A brief discussion of the sensitivity of the budget results to this partitioning is given in sections 5 and 6b.

d. Thermodynamic data

The environment of the squall line is that portion of the total area in Fig. 1 ahead of and behind the squall line not covered by clouds and precipitation. The mean thermodynamic properties of the squall line's environ-

[3] Extended Velocity Azimuth Display (Srivastava et al. 1986).

[4] A secondary maximum of reflectivity, or secondary band, is frequently observed within the stratiform region behind the convective line (Houze et al. 1990).

ment were calculated by averaging six soundings,[5] three ahead and three behind the squall line (Fig. 6). These six soundings were used so that the environmental thermodynamic profiles reflected the average conditions of the baroclinic environment in which the storm formed.

The mean thermodynamic properties of the convective updrafts and downdrafts were estimated from the two-dimensional thermodynamic and microphysical retrieval results of Braun and Houze (1994). Two sets of thermodynamic profiles were estimated: one for the updrafts and one for the downdrafts. For the updraft profiles, the retrieved thermodynamic fields were averaged over the convective region [see Figs. 3b and 6a,c of Braun and Houze (1994)] where $w > 0$. For the downdraft profiles, the data were averaged over the convective and transition zone[6] regions where $w < 0$. The transition zone was included so that data were available at middle and upper levels. The updraft and downdraft thermodynamic profiles are shown in Fig. 7 as perturbations from the environmental profiles (Fig. 6). The mean updraft and downdraft temperatures are similar above 3 km, but the mean downdraft temperatures are cooler below this level. The main difference between the two profiles is the drier conditions in the downdraft sounding below ~7 km. Updraft temperature perturbations at low levels are negative because the thermodynamic retrieval was unable to resolve the sharp temperature gradients at the leading edge of the cold pool.[7] While the low-level temperature perturbations were generally negative, they approached zero within the convective updraft (see Fig. 6a of Braun and Houze 1994).

A sounding taken within the stratiform region, before the secondary maximum of radar reflectivity had developed, is used to characterize the thermodynamic conditions in the stratiform region in the early stage. These thermodynamic profiles (dot-dashed lines in Fig. 7) are highly consistent with the average CP-3 vertical motion profile. Near 6 km, a stable layer (evident in a skew $T-\log p$ plot, not shown) separated air with generally weak positive temperature perturbations in the ascending front to rear flow aloft from the cooler air in the descending rear inflow below (~3–6.5 km). The downdraft layer between 4.5 and 6.5 km was near saturation. Evaporatively cooled air in this layer was negatively buoyant, and a maximum of descent was near 4 km. Below this height, descent led to strong adiabatic warming and drying. The warming weakened the descent. As the drying effect of the descent weakened, evaporation apparently moistened the layer near 2 km.

Thermodynamic profiles for the stratiform region at the mature stage (dashed line in Fig. 7) were constructed from low-level soundings[8] (below 500 mb) taken within the region of the secondary maximum of reflectivity and from the thermodynamic retrieval data (above 500 mb) of Braun and Houze (1994). The temperature perturbations show a deep layer (from the surface to 5 km) of air colder than the environmental temperatures. Above 5 km, the temperatures were up to 3 K warmer than the environment. Apparently, during the period between the early and mature stages, significant warming occurred by detrainment of sensible heat from the convective region and latent heating associated with condensation and deposition in mesoscale ascent above 5 km. Below 5 km, strong cooling occurred as a result of melting and evaporation (Braun and Houze 1995b).

Thermodynamic conditions within the anvil region (not shown) were obtained by averaging six soundings[9] taken behind the stratiform region. Storm-relative winds and dewpoint temperature profiles indicated that dry rear inflow was entering the back of the stratiform region between roughly 3.7 and 7.4 km.

4. Methodology

a. *Estimating* $\bar{c}$, $\bar{e}$, $\bar{b}$, and $\bar{s}$

The net heating rates associated with condensation, evaporation, deposition, and sublimation are estimated by two methods. The first method uses the equation for conservation of water vapor:

$$L_v(\bar{c} - \bar{e}) + L_s(\bar{b} - \bar{s}) \approx - L\sigma_{\rm cl}\bar{w}_{\rm cl}\frac{\partial \bar{q}_{\rm cl}}{\partial z}, \quad (4)$$

where $q_{\rm cl}$ is the water vapor mixing ratio in the cloudy region, and $L = L_v$ for $T \geq 0$°C or L_s for $T < 0$°C. Equation (4) assumes that the dominant balance in the water vapor budget is primarily between the microphysical processes and vertical advection. We show below that this assumption is not valid in the stratiform precipitation region, where the effects of horizontal advection and eddy moisture fluxes become important relative to vertical advection.

The second method uses the thermodynamic equation. The heating is approximated by the vertical advection of in-cloud dry static energy:

[5] The locations and times of the soundings are Russell (RSL), Kansas, at 0430 and 0555 UTC, Pratt (PTT), Kansas, at 0600 UTC, McConnell Air Force Base (IAB), Kansas, at 0130 UTC, Enid (END), Oklahoma, at 0134 UTC, and Oklahoma City (OKC), Oklahoma, at 0230 UTC.

[6] The region of minimum low-level radar reflectivity located between the leading convective line and the secondary maximum of reflectivity in the trailing stratiform region.

[7] The horizontal resolution of the dual-Doppler wind fields used in the retrieval was 3 km.

[8] PTT at 0305 UTC, IAB at 0431 UTC, and END at 0428 and 0543 UTC.

[9] RSL at 0250, 0430, and 0555 UTC, PTT at 0430 and 0600 UTC, and Dodge City, Kansas, at 0238 UTC.

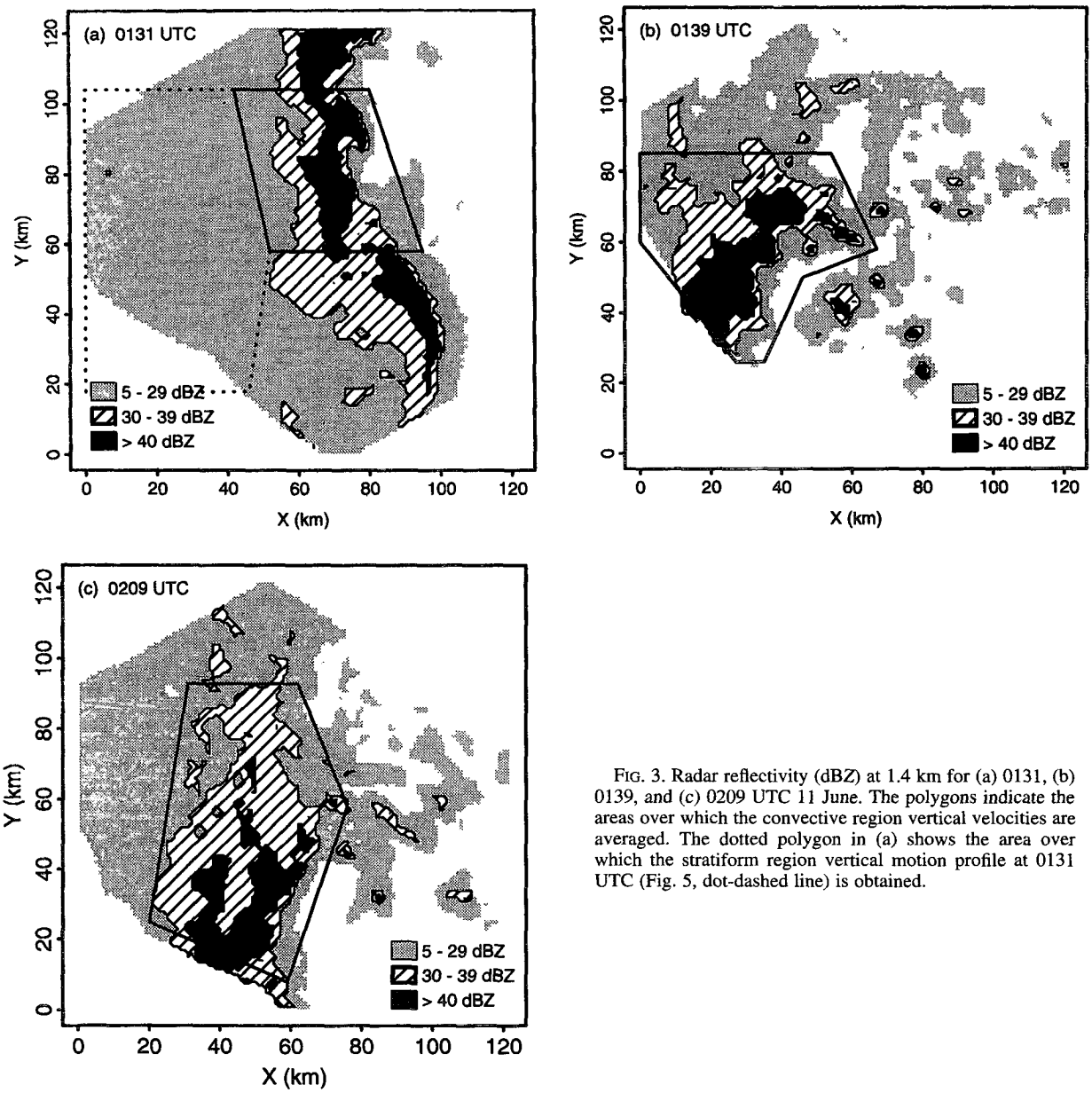

FIG. 3. Radar reflectivity (dBZ) at 1.4 km for (a) 0131, (b) 0139, and (c) 0209 UTC 11 June. The polygons indicate the areas over which the convective region vertical velocities are averaged. The dotted polygon in (a) shows the area over which the stratiform region vertical motion profile at 0131 UTC (Fig. 5, dot-dashed line) is obtained.

$$L_v(\bar{c} - \bar{e}) + L_s(\bar{d} - \bar{s}) + L_f(\bar{f} - \bar{m}) + \sigma_{cl}Q_{rcl} \approx \sigma_{cl}\bar{w}_{cl}\frac{\partial \bar{s}_{cl}}{\partial z}. \quad (5)$$

Since the heating and cooling rates associated with freezing, melting, and radiative processes are known (see below), the net heating associated with the remaining terms on the left side of (5) can be determined. The calculation of $\bar{f}$, $\bar{m}$, and Q_{rcl} is discussed in the next two subsections.

The contributions of the convective and stratiform regions to the averages in (4) and (5) are subdivided into contributions by updrafts and downdrafts in each region. For the convective region, we use dual-Doppler synthesized vertical velocities, which resolve the convective-scale updrafts and downdrafts; hence, the separate contributions of updrafts and downdrafts are readily determined. For the stratiform region, we use the EVAD vertical velocities, which represent temporal averages of areal means over 40-km diameter circles enclosing the radar. Thus, the EVAD data do not resolve the convective-scale motions within the stratiform region but rather represent areal-mean vertical motions in the stratiform region. Stratiform region heating

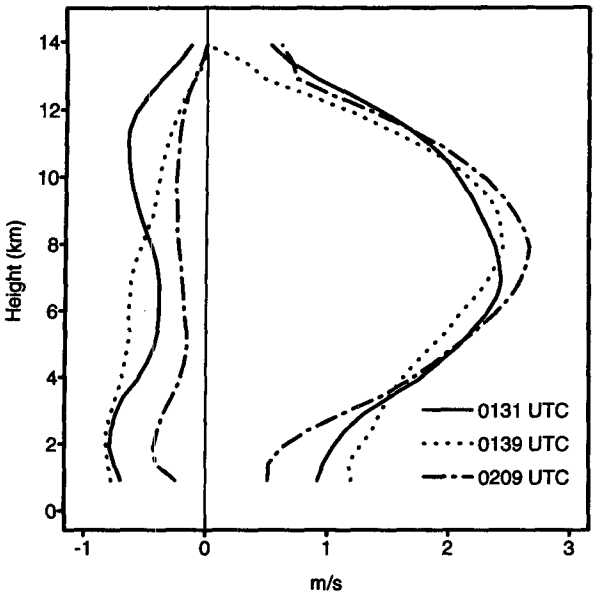

FIG. 4. Profiles of mean updraft and downdraft vertical velocities for the convective regions shown in Fig. 3.

rates from (4) and (5) are calculated using these stratiform region mean vertical velocities and thermodynamic conditions.

The applicability of (4) and (5) was tested by using output from a two-dimensional, nonhydrostatic cloud model simulation of the 10–11 June squall line (Yang and Houze 1995a). The fields of rain and snow mixing ratios and vertical velocity at 632 min in the simulation are shown in Fig. 8. Instantaneous model latent heating rates at 632 min were averaged over the convective updrafts and downdrafts (x = 155 to 210 km in Fig. 8) and over the stratiform region (updrafts and downdrafts combined, x = 60 to 154 km in Fig. 8). Area-mean latent heating rates involving water vapor (associated with c, e, $\mathfrak{d}$, and $\hat{s}$) are indicated by the solid lines in Figs. 9a and 9c, while the total latent heating rates (associated with c, e, $\mathfrak{d}$, $\hat{s}$, f, and m) are indicated by solid lines in Figs. 9b and 9d. In Figs. 9a and 9c, the dotted lines indicate the vertical advection term on the right side of (4), while in Figs. 9b and 9d, the dotted lines indicate the vertical advection term in (5).

For the convective region, the profiles in Fig. 9 suggest that the right-hand side of (4) provides a better estimate of the average latent heating rate than the right-hand side of (5). It yields both the correct magnitude of the area-mean heating rate and provides a better estimate of the level of maximum heating. In the stratiform region, the cloud model data suggests that the vertical advection of water vapor (4) only roughly

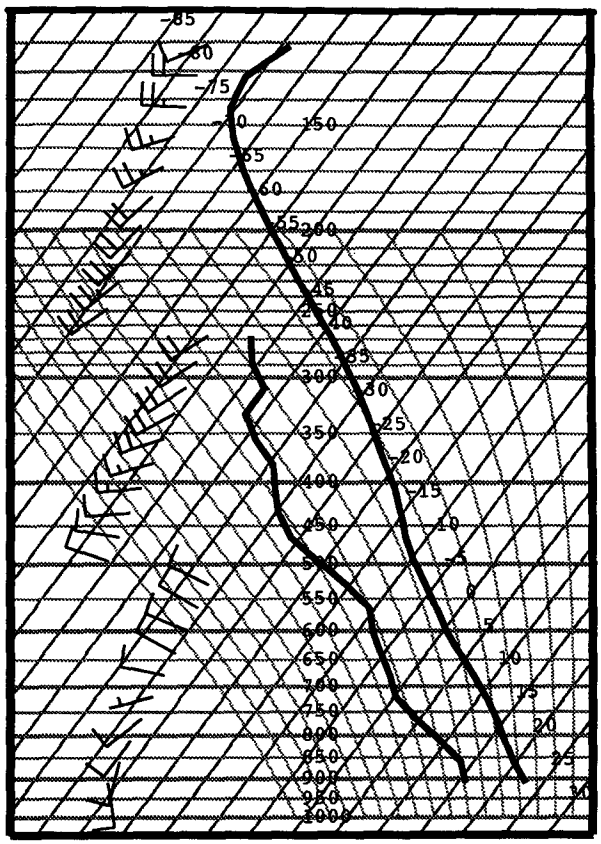

FIG. 6. Skew T–log$p$ sounding depicting the squall line environment. Full wind barb = 5 m s^{-1}, half barb = 2.5 m s^{-1}.

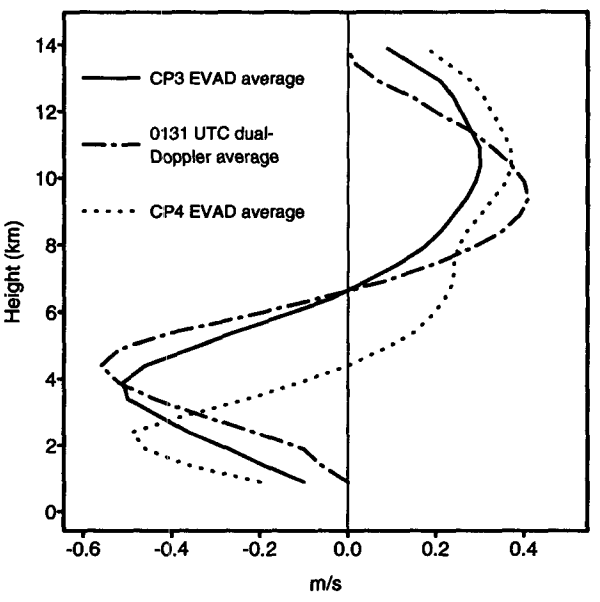

FIG. 5. Average stratiform-region vertical motion profiles determined from the EVAD method for the CP-3 and CP-4 radars and from the dual-Doppler analysis at 0131 UTC (dotted polygon in Fig. 3a). The CP-3 and CP-4 profiles are from Fig. 15 of Rutledge et al. (1988).

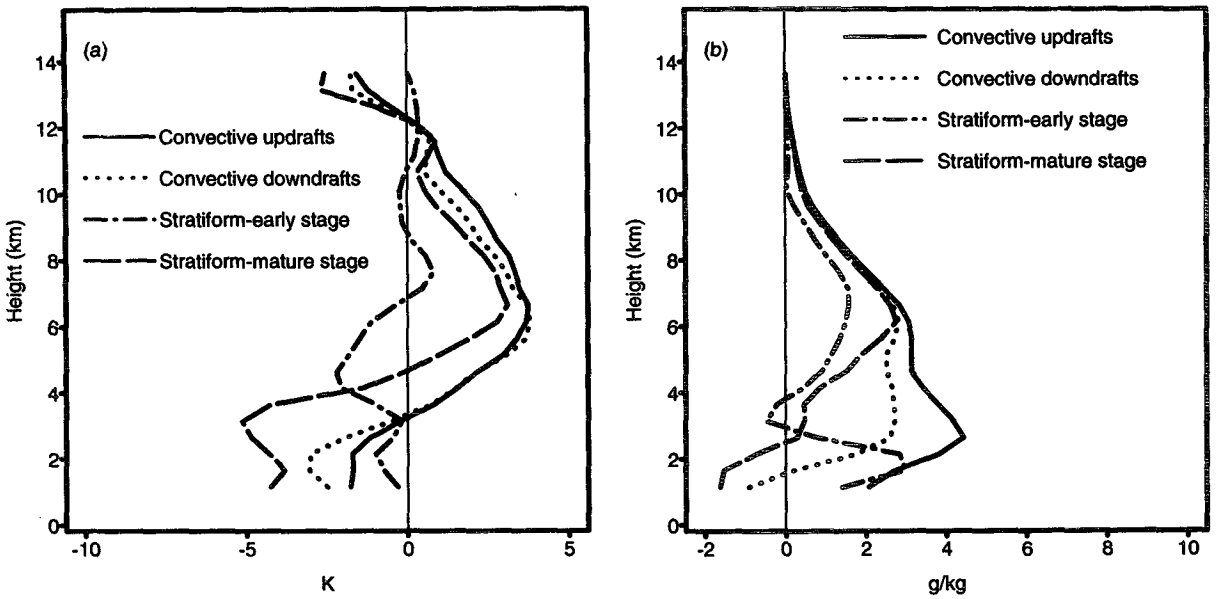

FIG. 7. (a) Temperature and (b) water vapor mixing ratio perturbations (from the environmental thermodynamic profiles, Fig. 6) for convective updrafts and downdrafts and the early and mature stage stratiform precipitation regions.

represents the profile of latent heating. On the other hand, the total latent heating is well approximated by the vertical advection of dry static energy in (5). The poor performance of (4) in the stratiform region results from the neglect of horizontal advection of water vapor and eddy moisture fluxes, which are significant in this region.

Very similar results regarding the validity of (4) and (5) were obtained when the same calculations were made at other times between 632 and 660 minutes of the simulation. We therefore use (4) to diagnose convective-region heating rates and (5) to diagnose stratiform-region heating rates. The condensation and evaporation terms in the water budget (C_{cu}, E_{cd}, C_{su}, and E_{sd}) are determined by vertically integrating the condensation and evaporation rates calculated from (4) in the convective region and (5) (after subtracting the freezing, melting, and radiative heating rates) in the stratiform region.

b. *Melting and freezing rates*

Braun and Houze (1995b) showed that the cooling by melting was significant in both the convective and stratiform precipitation regions of the 10–11 June storm. Therefore, it is necessary to include estimates of the cooling rates for both regions in the heat budget. For the stratiform region, the cooling by melting can be estimated from radar reflectivity profiles (Leary and Houze 1979). However, to extend the calculations to the convective region, a numerical model is needed to retrieve the cooling rates. Freezing rates for the convective region are also needed. Chong and Hauser (1990) and Braun and Houze (1995b) have applied thermodynamic and microphysical retrieval models to determine heating rates from dual-Doppler-radar data. These methods find the optimal balance between the observed kinematic fields and retrieved microphysical variables and represent a direct means of obtaining heating rates from radar observations. In this study, we obtain the melting and freezing rates through a retrieval of vertical profiles of the microphysical variables and microphysical processes from vertical profiles of vertical velocity (Braun and Houze 1995a). The equations governing the conservation of each water substance are area-averaged and expressed in terms of the area-mean vertical velocity and water mixing ratio. Parameterization of microphysical processes (similar to Lin et al. 1983) allows for the determination of the mixing ratio variables given profiles of area-mean vertical velocity, temperature, and pressure. Solution of the equations requires the assumption of stationarity of the *area-mean* cloud and precipitation mixing ratios but not a steady state at every grid point. The convective region satisfied this requirement approximately for the times considered here. The stratiform precipitation region satisfied the stationarity assumption during the mature stage (0330–0530 UTC) but, as will be shown in the water budget analysis, this assumption was not valid during the early stages of the squall line (0030–0230 UTC), during which time the area-mean mixing ratios in the stratiform region were increasing.

For the convective region, we apply the one-dimensional model to the three vertical profiles of mean vertical velocity based on dual-Doppler-radar wind fields. Thermodynamic profiles (temperature and pressure)

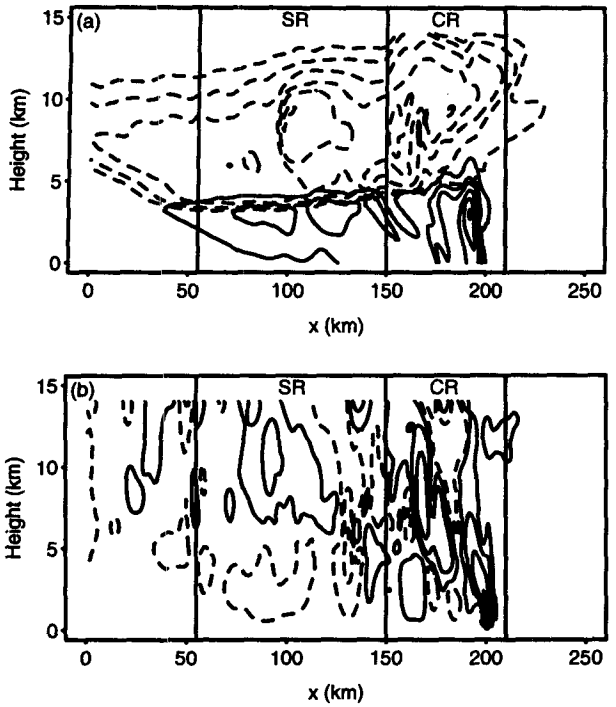

FIG. 8. Cross sections of (a) rain and snow mixing ratios and (b) vertical velocity at 632 min in the two-dimensional simulation of Yang and Houze (1995a). Contours for rain are drawn at 0.1, 0.5, 1, 2, 3, and 4 g kg^{-1} and for snow at 0.5, 1, 2, 4, 6, and 8 g kg^{-1}. Contours for vertical velocity are drawn at ± 0.5, 2, 5, and 10 m s^{-1}. Vertical lines mark the convective region (CR) and stratiform region (SR).

are obtained from a convective-region average of the retrieved thermodynamic fields of Braun and Houze (1994). For the stratiform region, melting rates could not be obtained for the early stage because of the lack of stationarity of the area-mean mixing ratios (see section 6a). For the mature stage, the CP-4 mean vertical velocity profile is used to estimate the melting rates. Thermodynamic data correspond to the dashed lines in Fig. 7.

c. *Radiative heating rates*

Longwave heating and cooling rates are estimated by applying the two-stream plane-parallel multiband radiative transfer model of Stackhouse and Stephens (1991) and Wong et al. (1993) to the retrieved microphysical fields. Solar heating rates are negligible since the solar zenith angle exceeded 80° for the earliest times considered here. Cloud and precipitation particle optical properties (attenuation coefficient, single-scattering albedo, and asymmetry factor) are estimated from Mie theory by assuming equivalent diameter spheres and using the particle size distributions specified in the microphysical retrieval. Table 3 summarizes these size distributions.

The radiative transfer model is applied to vertical profiles of the mixing ratios of the microphysical variables (cloud water and ice, rain, and precipitation ice) obtained from the one-dimensional retrieval model (and used to estimate the melting and freezing rates). For the convective and stratiform regions, hydrometeor profiles are derived from mean vertical motions in the respective areas, as noted in section 4b. Since accurate vertical motions in the anvil region are unavailable, the vertical profile of cloud ice in the stratiform region at the mature stage is used to describe the microphysical characteristics of the anvil. Precipitation-sized particles in the anvil are neglected.

The plane-parallel assumption for the radiative transfer model allows us to estimate the area-mean bulk radiative heating rates from vertical profiles of the hydrometeor fields. Under the plane-parallel assumption, resolved horizontal inhomogeneities do not impact the radiative fluxes within a given vertical column. Hence, the radiative heating rates depend only on the microphysical characteristics of the column. In stratiform precipitation, where the microphysical properties tend to be relatively uniform, the heating rates determined from area-mean profiles of the microphysical variables (from the one-dimensional model) should be nearly equivalent to the area-mean heating rates estimated by averaging heating rates determined in each vertical column within the region from two- or three-dimensional data.

In the convective region, where large variations in the microphysical fields exist, it is not clear that area-mean heating rates can be determined from area-mean vertical profiles of the microphysical fields. However, as will be shown in section 6, the radiative heating rates in the convective region are generally negligible compared to the latent heating rates, so the effects of neglecting spatial variability in the convective region are not important to our conclusions.

Tests of the sensitivity of the radiative transfer model to the microphysical profiles were performed for the stratiform region (Fig. 10). The vertical velocity profile and sounding used in the stratiform-region retrieval are in Figs. 5 (dotted line) and 7 (dashed lines). The calculated radiative heating rates are most sensitive to the cloud ice profile. One source of uncertainty in the radiative heating rates is in the one-dimensional retrieval model. Because the upper boundary condition for cloud ice is specified (usually assumed to be zero), the cloud ice profile is truncated at upper levels. The sudden truncation of the cloud ice mixing ratios in the upper troposphere has a significant impact on the resultant cloud-top cooling rates. Figure 11a shows radiative heating rates for three cases. In the first case (control case, solid line), the cloud ice profile is from the retrieval model without modification. In the second and third cases (Test 1 and Test 2), the cloud ice profile is linearly interpolated to one and two grid levels, respectively, above the uppermost level with nonzero

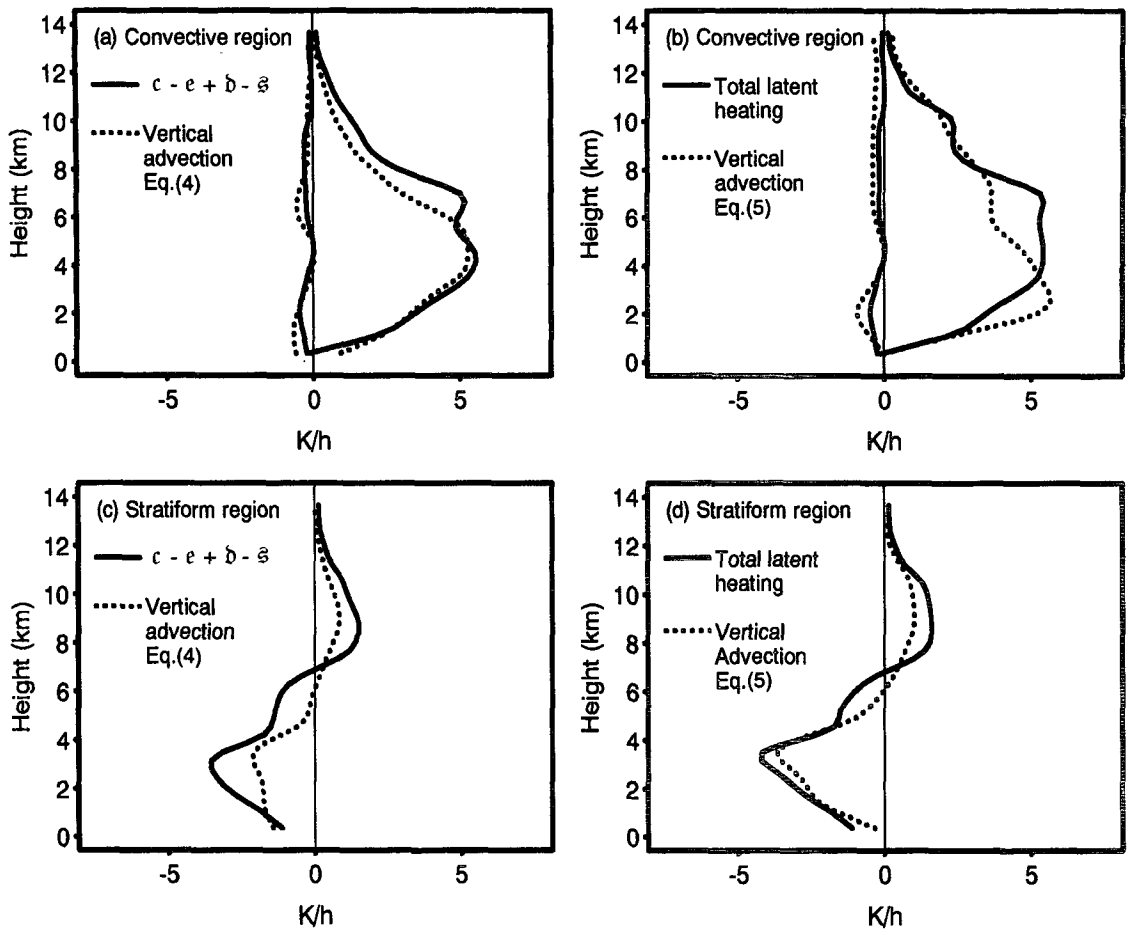

FIG. 9. Profiles of average latent heating rates and estimated heating rates from area-averaged vertical velocity and thermodynamic data for convective updrafts and downdrafts in (a) and (b) and for the stratiform region (updrafts and downdrafts combined) in (c) and (d) from the simulation of Yang and Houze (1995a). Solid lines indicate profiles of heating associated with c, e, b, and s in (a) and (c) and c, e, b, s, f, and m in (b) and (d). Dotted lines indicate heating rates calculated according to (4) in (a) and (c) and (5) in (b) and (d).

cloud ice mixing ratio. These cases represent a more gradual decrease in cloud ice. Figure 11a indicates that as the cloud ice profile decreases more gradually, the radiative cooling spreads out through a deeper layer and is weaker than in the control case. Since a more gradual decrease in cloud ice is probably more realistic, we perform the radiative calculations as in Test 2—cloud ice mixing ratios linearly interpolated to two grid levels above the uppermost level with nonzero cloud ice from the retrieval model.

The radiative heating rates are also sensitive to the assumed size of the cloud ice particles. Figure 11b shows the radiative heating rates produced by the radiative transfer model for cloud ice particles with radii ranging from 50 to 200 μm. The profile corresponding to 50 μm is the same as Test 2 in Fig. 11a. The cloud-top cooling rates become stronger as the size of the particles decreases. To avoid underestimating the cooling rates, we assume a cloud ice radius of 50 μm.

TABLE 3. Size distributions and mean diameters assumed for the calculation of optical properties used in the radiative transfer model.

	Distribution	Mean diameter (mm)
Cloud water	Monodisperse	0.02
Cloud ice	Monodisperse	0.10
Rain	Exponential	0.54
Precipitation ice	Exponential	1.00

d. Eddy sensible heat fluxes

The convergences of the eddy sensible heat flux [last term on the right of (3)] were calculated using the mean vertical velocity profiles in Figs. 4–5 and the temperature perturbation profiles in Fig. 7a.

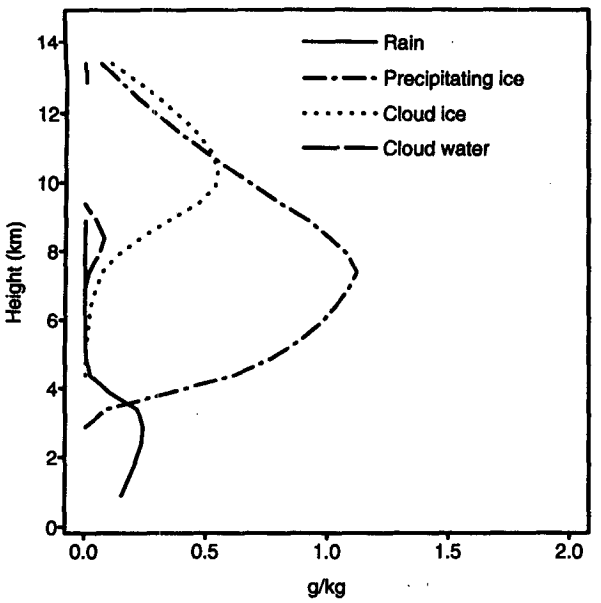

FIG. 10. Vertical profiles of area-averaged mixing ratios for rain, precipitating ice, cloud water, and cloud ice determined from the one-dimensional retrieval method of Braun and Houze (1995a) for the stratiform region. Input for the retrieval were obtained from the CP-4 vertical velocity profile in Fig. 5 (dotted line) and the mature-stage stratiform-region thermodynamic profiles in Fig. 7 (dashed lines).

5. Water budget

For the early stage, R_c and R_s are determined from the PAM/SAM station raingauge data (Table 2), and C_{cu}, E_{cd}, C_{su}, and E_{sd} are determined from the mean vertical velocity profiles. To solve for the other variables, we assume that C_{af} is a small percentage of C_{cu}, as in Leary and Houze (1980). We let $C_{af} = 0.025C_{cu}$. Furthermore, we assume that the total water content of the convective region is steady so that the storage term S_c is zero. Then C_a can be determined from (1). In the stratiform region, C_a is now known, so we can solve for the quantity $(C_{ar} + S_s)$ from (2).

Table 4 shows the values of the water budget parameters for the early stage. During this period 85% of the total rainfall was convective, 22% of the condensate produced in the convective updrafts was evaporated in downdrafts, 35% fell out as convective rainfall, and 41% was advected into the stratiform region. The total source of condensate in the stratiform region $(C_a + C_{su})$ was dominated by the transport of condensate from the convective region (87%), in general agreement with the model results of Tao et al. (1993) and in very good agreement with the kinematic and dynamic modeling study of Gallus (1994). Nearly one-half (43%) of the total input into the stratiform region was evaporated in the mesoscale downdraft, 17% fell out as stratiform rainfall, while 43% was transported into the rear anvil or was stored within the stratiform region. The large value of $(C_{ar} + S_s)$ is consistent with the observations that the total water content (radar reflectivity) of the stratiform region and the size of the anvil were increasing during this period. Consequently, the one-dimensional microphysical retrieval calculations cannot be performed for this period in the stratiform region.

During the mature stage, the rear anvil was no longer expanding and the water content of the stratiform region (as inferred from the radar reflectivities) was approximately stationary. Therefore, we assume that $S_s = 0$ and that C_{ar} is relatively small. Here we assume that C_{ar} is 5% of the total source of condensate in the stratiform region $(C_a + C_{su})$. Note that our assumption that C_{ar} is small produces a conservative estimate of C_a. If C_{ar} is greater than that assumed (more transport into the rear anvil), then C_a must be greater in order to balance the budget. The terms C_{su} and E_{sd} are determined from an area-weighted average of the CP-3 and CP-4 water budgets, with CP-3 and CP-4 contributing 20% and 80%, respectively, to the total stratiform region budget. Term C_a can then be determined from (2). To test the sensitivity of the results to this partitioning of the stratiform region, water budgets were also estimated by assuming that CP-4 represented 60% and 100% of the stratiform precipitation area. The differences from the original calculations averaged 6% for C_{su}, 5% for C_a, and 1% for E_{sd}.

For the convective region during the mature stage, we assume that $C_{af} \approx 0$, since the forward anvil was also no longer expanding, and that S_c is also zero. During this period, information on the convective region vertical motions is unavailable. Hence, C_{cu} and E_{cd} are unknown. However, the net condensation $(C_{cu} - E_{cd})$ can be determined from (1) since R_c and C_a are known. If we assume that the vertical profiles of heating in the convective region are similar to the early stages, but that the magnitudes of the heating rates have changed by a constant factor φ, then C_{cu} and E_{cd} can be estimated. Let $(C_{cu} - E_{cd})_1 = R_c + C_a$ be the net condensation determined from the mature-stage convective rainfall and the stratiform region water budget parameters and $(C_{cu} - E_{cd})_2$ be the net condensation determined from the early-stage convective-region mean vertical velocities. Then $\varphi = (R_c + C_a)/(C_{cu} - E_{cd})_2$ and $(C_{cu})_1 = \varphi(C_{cu})_2$ and $(E_{cd})_1 = \varphi(E_{cd})_2$. The factor φ is used to scale the mature-stage convective-heating profiles in section 6b and has a value of 0.87.

The water budget parameters for the mature stage are also shown in Table 4. During this period, the stratiform rainfall accounted for 30% of the total rainfall. The condensate produced in the mesoscale updraft had increased and the flux from the convective region had decreased such that the horizontal transport of condensate from the convective region accounted for 65% of the total source of condensate. This value is in good agreement with Gallus's (1994) results for the intermediate period of his simulation, but exceeds the mature stage values of ~38% found in the cloud modeling study of Tao et al. (1993) and ~46% in the rawinsonde

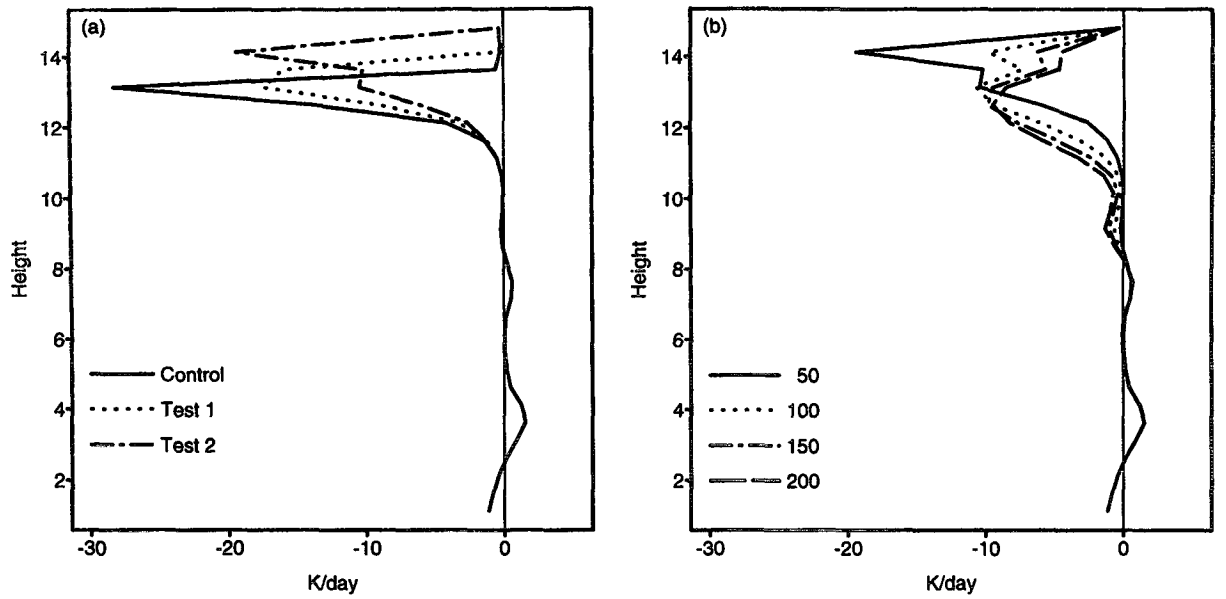

FIG. 11. Longwave cloud-top cooling rates (K d^{-1}) for the stratiform region. (a) The solid line indicates the cooling rates for the unmodified cloud ice profile (Fig. 10). Tests 1 and 2 are cooling rates for cases in which the cloud ice profile is extended vertically one and two grid points, respectively, as described in the text. (b) Cooling rates (K d^{-1}) for assumed cloud ice particle radii ranging from 50 to 200 μm.

composite study of GJ. The discrepancy in the contribution of C_a to the total stratiform condensate source between the GJ result and the radar-derived value may be caused by several factors. First, GJ estimated C_a by using a relationship between radar reflectivity and precipitation ice mass and assuming a mean radar reflectivity of 25 dBZ based on radar reflectivities at the rear of the convective region at 0400 UTC. Errors in precipitation ice content estimated by this manner could readily account for the difference. Second, we assumed that the CP-3 and CP-4 vertical motion profiles, obtained in the northern portion of the stratiform region, were representative of the entire stratiform precipitation region. If the mesoscale descent was, for example, weaker in the southern portion of the squall line, then our estimate of E_{sd} and, consequently, C_a would be too large. Third, the water budget in GJ corresponded to a slightly later period (0430–0730 UTC) than in our analysis. The rapid weakening of the convective line after 0600 UTC (Fig. 2) may have contributed to the lower value of C_a in their budget. Finally, although it was much less a problem at 0600 than at 0300 UTC, aliasing of convective motions into the stratiform region may also have contributed somewhat to the difference by causing an overestimate of C_{su}. Of the total input of condensate in the stratiform region calculated in this study, 59% was evaporated in the mesoscale downdraft and 35% fell as precipitation.

TABLE 4. Water budget parameters for the 10–11 June storm for the early and mature stages expressed as a percentage of the total rainfall for the respective stage. Values have been rounded to the nearest 5%. The letter T denotes the 16-h average values from a simulation of the 10–11 June squall line by Tao et al. (1993). The GJ values are from Gallus and Johnson's (1991) rawinsonde composite for 0600 UTC 11 June.

Convective	R_C	C_{cu}	E_{cd}	C_{af}	C_a
Early	0.85	2.45	0.55	0.05	1.00
Mature	0.70	1.60	0.35	0.	0.55
T 16-h average	0.81	1.03 (net)	—	0.	0.21
Stratiform	R_S	C_{su}	E_{sd}	$C_{ar} + S_s$	C_a
Early	0.15	0.15	0.50	0.50	1.00
Mature	0.30	0.30	0.50	0.05	0.55
GJ 0600 UTC	0.30	0.30	0.15	0.11	0.26
T 16-h average	0.19	0.32	0.20	0.06	0.21

6. Heat budget

a. Early stage (0030–0230 UTC)

The convective heating and cooling rates [right side of (3)] were estimated by the methods described in section 4. Equation (4) was used with the mean vertical motions (Fig. 4) for each of the three convective region dual-Doppler volumes and the mean convective updraft and downdraft soundings (Fig. 7). These three sets of heating rates were then averaged to obtain the heating profiles shown in Fig. 12. Heating from condensation in the convective updrafts peaked near 5.4 km (~500 mb). Cooling by evaporation in the convective downdrafts was maximized near 1 km and decreased with increasing height. Strong cooling from melting occurred near 4.4 km and exceeded the cooling by evap-

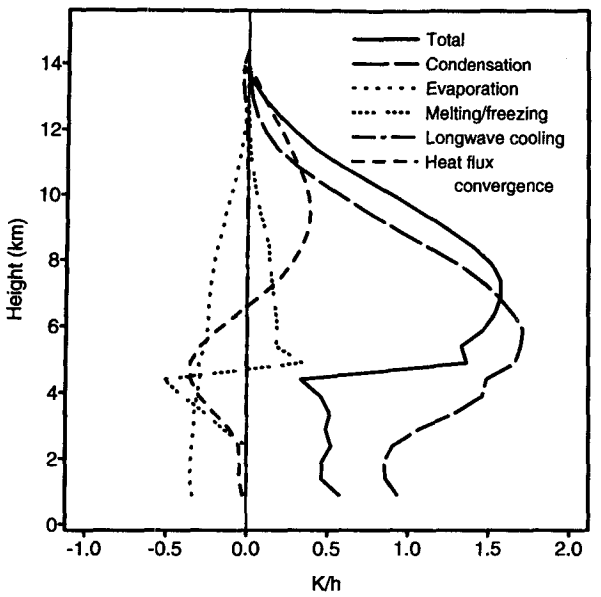

FIG. 12. Profiles of the area-weighted convective heating rates [e.g., $\sigma_c(\ )_c$] for each term on the right side of (3) during the early stage of the squall line.

oration at that level by more than 50%. The heating by freezing was small compared to condensation but was not negligible. The vertical eddy transport of heat produced cooling between 2 and 6.4 km and warming above 6.4 km. The cooling at cloud top associated with radiative processes was negligible.

The total convective heating profile (solid line in Fig. 12) shows maximum heating near 7.4 km. The combined effects of melting, evaporation, and convergence of the eddy heat flux produced a significant vertical gradient in heating, particularly in the 4–5-km layer. The sharp vertical gradient in heating at midlevels, and its near absence at low levels, implies that the maximum area-averaged convergence occurred at midlevels rather than near the surface. This result is consistent with vertical profiles of divergence within mature convective regions of MCSs in the Tropics (Mapes and Houze 1993, 1995) and in Florida (Yuter and Houze 1995).

Retrieval of microphysical profiles from the CP-3 vertical motion profile and the early-stage stratiform-region thermodynamic data (Fig. 7, dot-dashed lines) could not be performed for early stages because of the lack of stationarity of the mean precipitation mixing ratios during this period (see the water budget discussion in section 5); hence, freezing, melting, and radiative heating rates are not available. However, the consistency between the 0131 UTC dual-Doppler-derived mean vertical motion and the CP-3 average vertical motion (averaged over ~0254–0419 UTC) suggests that the mean vertical velocity varied more slowly than the mean microphysical profiles. We assume, therefore, that the stratiform region vertical motions, and thus the heating, were relatively stationary during this period. We calculate the mean stratiform-region heating using the CP-3 vertical motion profile (Fig. 5), the early-stage stratiform region thermodynamic data, and (5). Profiles of the total latent heating and the heating by the eddy heat flux convergence in the stratiform precipitation region for the early stages of the squall line are shown in Fig. 13. The significant kink in the cooling rate profile near 4 km is partially a consequence of estimating the heating based on independent measurements of the thermodynamic (from one sounding) and kinematic (from radar) fields. It may also be caused by the relatively unsteady nature of the stratiform region during this period. However, for our purposes, the total heating profile probably represents a reasonable estimate of the heating profile in the stratiform region at this early stage. The stratiform region was characterized by cooling within a deep layer from the surface to near 6 km (400 mb), with relatively weak heating in the mesoscale updraft above 6 km.

Only radiative processes were considered within the anvil. The profile of cloud ice mixing ratio (see Fig. 10) determined from the CP-4 mean vertical motions and the rear anvil thermodynamic data were used to estimate the longwave heating and cooling within the anvil cloud. These heating rates are indicated in Fig. 14. Longwave cooling of about -17 K d^{-1} occurred near cloud top, comparable in magnitude to the longwave cooling rates within the convective (not shown) and stratiform (Fig. 11) precipitation regions. Warming occurred within the lower half of the ice cloud

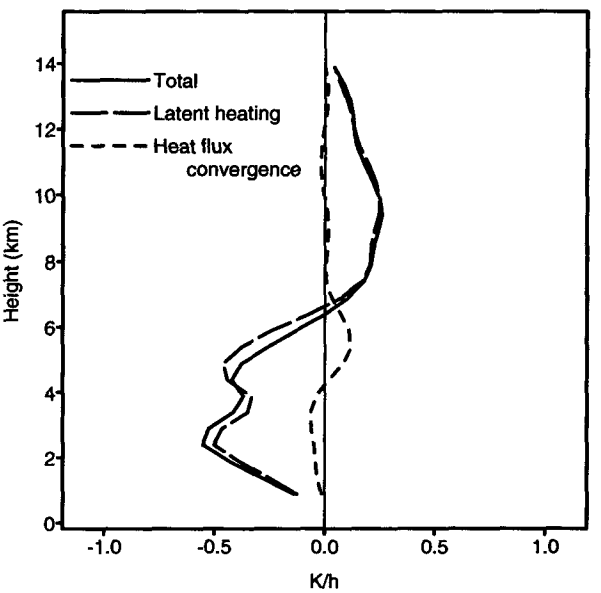

FIG. 13. Profiles of the area-weighted stratiform (CP-3) latent heating rates from (5), the convergence of the eddy sensible heat flux, and the total heating during the early stage of the squall line.

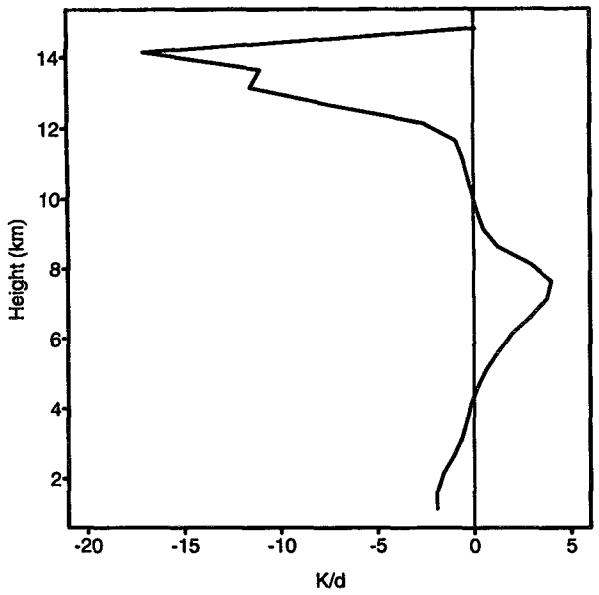

FIG. 14. Radiative heating rates for the anvil region based on the retrieved cloud ice profile in Fig. 10 and the rear anvil thermodynamic profiles.

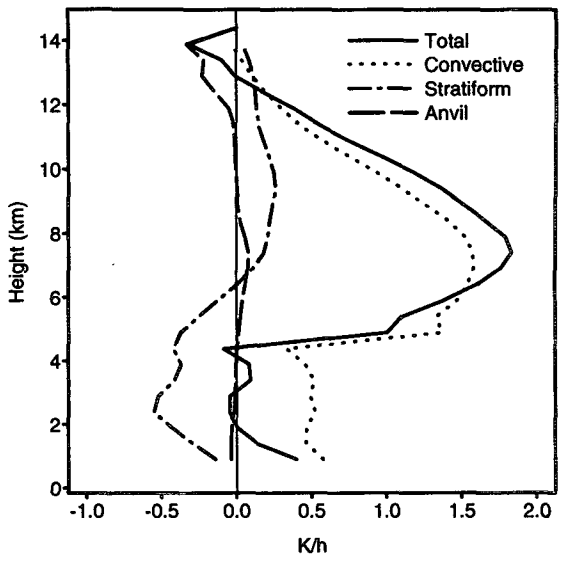

FIG. 15. Total heating of the large-scale area A for the early stage (solid line). Also shown are the area-weighted average heating rates in the convective ($\sigma_c Q_{1c}$), stratiform ($\sigma_s Q_{1s}$), and anvil ($\sigma_a Q_{1a}$) regions.

layer. The differential heating of the anvil cloud implies that the layer was being destabilized by radiative processes, which contributed to the maintenance of the cloud (Lilly 1988).

Figure 15 shows the total heating within the large-scale area during the early stage of the squall line. The area-weighted average heating rates in the convective, stratiform, and anvil regions are also shown (i.e., $\sigma_c Q_{1c}$, $\sigma_s Q_{1s}$, and $\sigma_a Q_{1a}$). Below 4.4 km (~600 mb), the heating within the convective region was nearly canceled by evaporative cooling within the stratiform region (as suggested by Houze 1982). As a result, the net heating was confined largely to an 8 km (~400 mb) deep layer between 4.4 and 12.4 km (600 and 200 mb), with peak heating near the 7.4-km (400 mb) level. The heating at upper levels was dominated by the convection since the mesoscale updraft was relatively weak during this period. Because of the extensive anvil, strong radiative cooling was seen near cloud top. Therefore, while radiative processes were of minor importance within the precipitation regions compared to latent heat release, radiative processes in the extensive nonprecipitating anvil region were significant and dominated the total heating within a shallow layer (~1.5 km deep) near cloud top.

b. Mature stage (0330–0530 UTC)

Heating rates for the secondary band portion of the stratiform region (i.e., for the CP-4 vertical velocity profile) during the mature stage are shown in Fig. 16. Compared to the early stage (Fig. 13), heating by condensation and deposition during the mature stage was stronger and occurred through a deeper layer than during the early stages. The minimum in heating near 12.5 km is an artifact of the retrieved temperatures from Braun and Houze (1994). At this level, the retrieved temperature profile became nearly adiabatic. As a result, the heating rates estimated from (5) were near

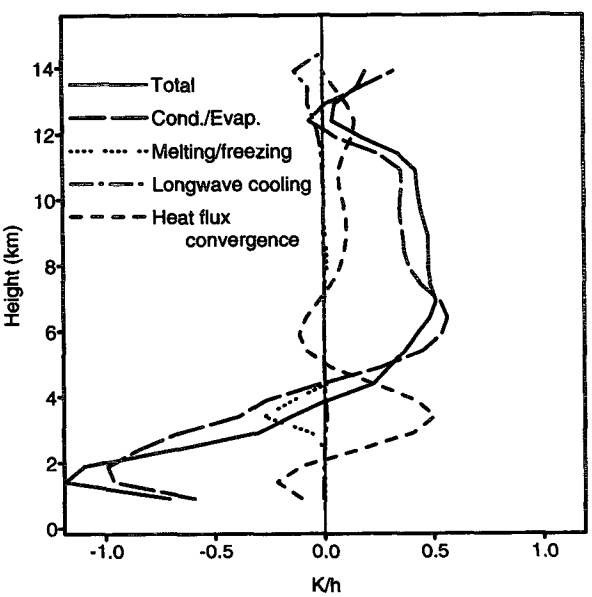

FIG. 16. Same as in Fig. 12 but for the secondary band portion of the stratiform region at the mature stage.

zero despite the presence of upward motion. Cooling by evaporation occurred within a shallower layer but was greater in magnitude, and the evaporation profile varied smoothly with height. This result is likely due to the relatively steady nature of the stratiform region during this period. Weak radiative cooling was offset by the heating from condensation and vertical eddy transports, which were much stronger during this stage than at the earlier times. In particular, the heating from eddy heat transports was maximized near the melting level and canceled the cooling by melting. The large increase in magnitude of the convergence of the eddy heat flux near the melting level resulted primarily from the substantial increase in the vertical gradient of temperature across the melting level (dashed line in Fig. 7a). The weaker peak in the convergence of the eddy heat flux near 12.5 km is produced by the large temperature gradient in the near-adiabatic layer described above.

The total heating rates for the mature stage and the area-weighted averages in the convective, stratiform, and anvil regions are shown in Fig. 17. The stratiform region profile in Fig. 17 is an area-weighted average of the CP-3 and CP-4 heating rate profiles. The heating rates in Fig. 16 (CP-4) are representative of about 80% of the stratiform area, while those in Fig. 13 (CP-3) are representative of 20% of the area. Assuming that the CP-4 profile represented 60% and 100% of the stratiform precipitation region produced maximum differences in heating rates of 0.2 K h^{-1} between 4–5.5 km and smaller differences at other levels. The convective region heating rates are similar to those in the early stage (Fig. 15) but have been weighted by a factor of 0.87 because of the water budget constraints described in the previous section. The anvil heating rates during the mature stage are slightly greater than those during the early stage because of the somewhat larger area of the anvil during the mature stage.

The heating rates for the mature stage of the squall line (Fig. 17) show distinct differences from those during the early stages (Fig. 15). In the mature stage, the total heating profile shows significant net cooling at low levels, as the cooling by evaporation in the stratiform region exceeded the low-level heating within convective updrafts. Above 500 mb, although the convective heating was assumed to be somewhat smaller than during the early stages (by a factor of 0.87), the total heating was somewhat greater because of the larger contribution of the stratiform region, which accounted for almost one-third of the total heating during the mature stage.

The heating rates estimated from radar data can be compared to the rates determined by GJ from lower-resolution composites of rawinsonde data. This comparison is complicated by the differences in time between their analyses (0300 and 0600 UTC) and our own (0030–0230 and 0330–0530 UTC). To minimize these differences, we compare radar-derived heating

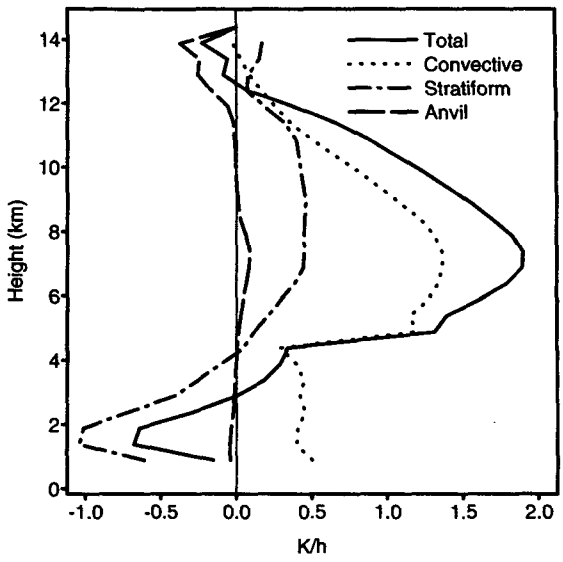

FIG. 17. Same as in Fig. 15 but for the mature stage.

rates averaged over 0030–0530 UTC to the 0300 UTC heating profiles of GJ (Fig. 18). Comparison to GJ's 0300 UTC profiles, rather than 0600 UTC, is necessitated by the lack of radar observations in the convective region beyond the early stage of the squall line. The GJ heating profile includes only the convective and stratiform precipitation regions (i.e., $\sigma_c + \sigma_s = 1$). Consequently, in Fig. 18, the radar-derived heating rates also include only the precipitation regions (i.e., the anvil region has been removed), and the lower axis has been scaled appropriately. The total heating rates estimated by the two very different methods are in agreement. However, between 1.5 and 4.5 km, the radar-derived total heating rates show weaker heating or stronger cooling than the GJ profile. As will be discussed in more detail below, this result has three potential causes: 1) the mesoscale downdraft cooling may be underestimated in GJ, 2) the mesoscale downdraft cooling may be overestimated in our results, and 3) low-level convective heating located ahead of the main precipitation region may have been unobserved by the radar.

Figures 18b and 18c show comparisons of the convective and stratiform components of the heating rates. Although the total heating profiles agree at upper levels, there is significant disagreement between the two estimates of the heating in the convective and stratiform regions. In the convective region, the heating at upper levels in GJ is much weaker (by about a factor of 2.5) than the radar-derived heating rates. In contrast, the stratiform heating rates of GJ are nearly a factor of 2.5 greater than our results. GJ suggested that the strong stratiform region heating rates were likely caused by aliasing of convective vertical motions into the stratiform region because the distance separating these

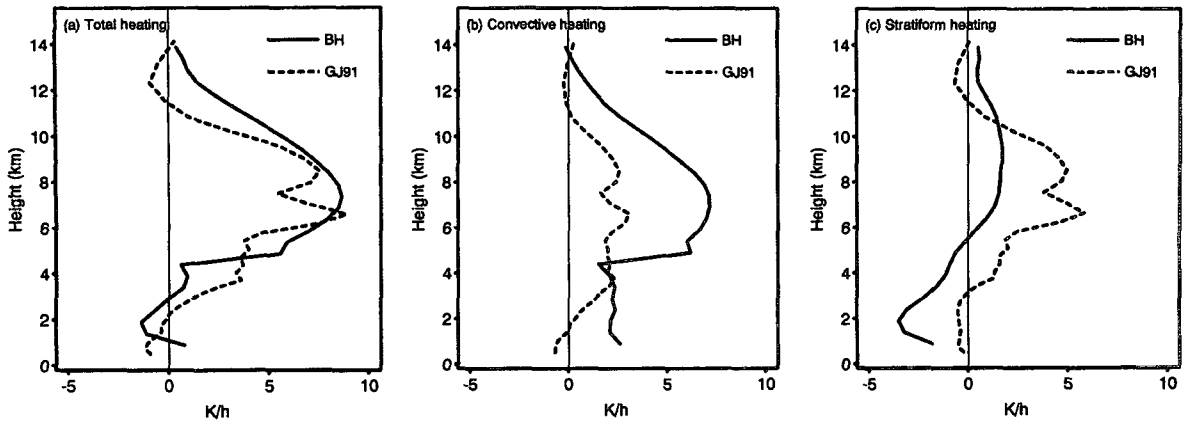

FIG. 18. Comparison of the radar-estimated (labeled BH) (a) total (convective + stratiform), (b) convective, and (c) stratiform heating rates averaged over the early (0030–0230 UTC) and mature (0300–0530 UTC) stages, with the corresponding heating rates from 0300 UTC from Gallus and Johnson (1991, labeled GJ91).

regions was small compared to the resolution of their analysis at this time. Also, the stratiform region was located close to the edge of the data network. The radar-derived heating rates quantify the errors associated with aliasing during the early to mature stage of the system since the radar data provide a better separation of the convective and stratiform heating. The larger separation of the convective and stratiform precipitation regions at 0600 UTC reduced the errors associated with aliasing (Figs. 9 and 10 of GJ), as manifested by a reduction (increase) of the stratiform (convective) region heating rates in GJ's 0600 UTC profiles. Thus, differences at mid to upper levels near 0300 UTC between the radar-derived heating rates and those of GJ are caused primarily by the limited horizontal resolution of the composited sounding data but would likely be reduced at later times.

The GJ stratiform profiles show only very weak stratiform cooling and convective heating at low levels, whereas the radar-derived rates are substantially stronger. The GJ cooling rates in the stratiform region and heating rates in the convective region were probably underestimated because of the coarse horizontal resolution of the sounding data. The canceling effects of the convective upward motions (aliased into the stratiform region) and the stratiform region mesoscale downward motions probably led to weaker diagnosed convective heating and weaker mesoscale cooling in their results.

It also appears that the radar-estimated cooling rates were overestimated. In our calculations, we assumed that the EVAD vertical motion profiles of Rutledge et al. (1988) were representative of the entire stratiform precipitation region. However, the large-scale composite of dual-Doppler and rawinsonde velocity data of Biggerstaff and Houze (1991a) and mesoscale model results of Zhang et al. (1989, their Fig. 19) suggest that the mesoscale descent in the southern portion of the squall line was weaker than that in the northern portion of the stratiform region.

The stronger low-level cooling seen in the total heating rates obtained from the radar data compared to GJ's profile may also be caused by our assumption regarding the shape of the mature-stage convective region heating profile and possibly by an undersampling of low-level convective updrafts located at the forward edge or ahead of the convective line. Low-level convective updrafts at their early stages may not contain sufficiently large hydrometeors to be detected by radar, and as a result these updrafts may not be included in the vertical motion profiles used to estimate the convective heating.

7. Potential vorticity budget

Since gradients of heating represent a major local source of potential vorticity[10] (PV), the effect of the squall line on the mesoscale to synoptic scale is probably most clearly defined in terms of the potential vorticity anomalies produced by the heating. HS91 examined the effects on PV of heating associated with a squall line by using distributions of heating that varied sinusoidally in the vertical. In this section, we use the convective and stratiform region vertical profiles of heating from the heat budget of the 10–11 June squall line to examine the effects of heating on the large scale from a PV standpoint. The heat budget results are used to define both the vertical distribution and the magnitude of the heating.

[10] As Haynes and McIntyre (1987) point out, PV is not created by the diabatic heating gradients but is diluted or concentrated by the diabatically induced influx of mass into an isentropic layer across its top and bottom.

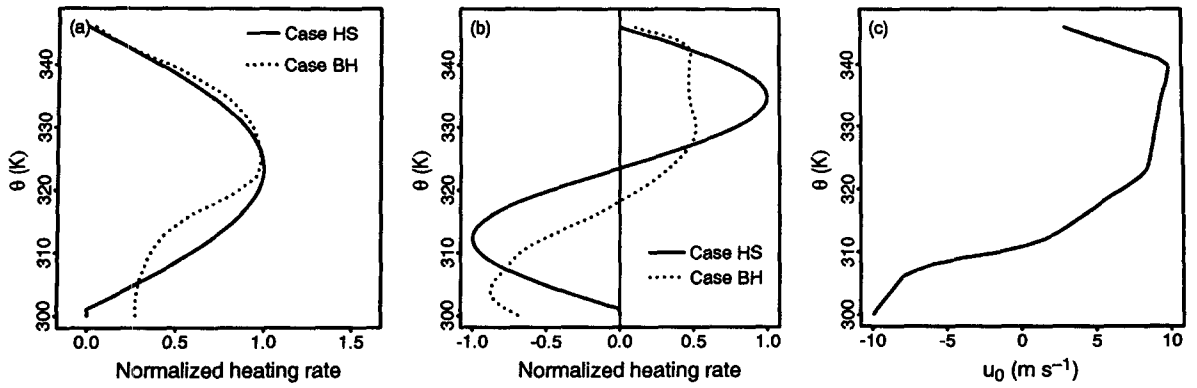

FIG. 19. Normalized vertical heating profiles [F in (7)] for (a) the convective region and (b) the stratiform region. (c) Basic state wind profile u_0 for Case BH. Case descriptions are given in the text.

The isentropic potential vorticity (P in equations, PV in the text) equation can be written as (Holton 1992, p. 112; Mapes and Houze 1993)

$$\frac{\tilde{D}P}{Dt} = \frac{P}{\sigma}\frac{\partial}{\partial\theta}(\sigma\dot{\theta}) - \sigma^{-1}\mathbf{k}\cdot\nabla_\theta \times \mathbf{M}, \qquad (6)$$

where $\tilde{D}/Dt = \partial/\partial t + \mathbf{V}\cdot\nabla_\theta$, $\mathbf{V}$ and ∇_θ are the horizontal velocity and gradient operator in isentropic coordinates, $P = \zeta_a/\sigma$, $\sigma = -g^{-1}\partial p/\partial\theta$, θ is potential temperature, $\dot{\theta}$ is the heating rate expressed as the time rate of change of θ, and ζ_a is the absolute vertical vorticity, $\zeta_\theta + f$, where ζ_θ is the relative vorticity in isentropic coordinates and f is the Coriolis parameter. The vector $\mathbf{M} = \dot{\theta}\partial\mathbf{V}/\partial\theta - \mathbf{F}$ is the apparent momentum source arising from vertical momentum transports and the forcing from subgrid-scale processes $\mathbf{F}$. The second term on the right of (6) combines the effects of vertical advection, vortex tilting, and subgrid-scale forcing. Expressed in this form, it produces PV anomaly couplets of opposite sign on either side of the vector $\mathbf{M}$. In other words, it represents a nonadvective horizontal flux of PV on an isentropic surface with the PV moving to the right of $\mathbf{M}$ (Haynes and McIntyre 1987), which is directed parallel to the shear vector and opposite $\mathbf{F}$. Equation (6) is similar in form to the vorticity equation that Mapes and Houze (1992, 1993) used to investigate the effects of heating and vertical momentum transports on the large-scale vorticity field in the Tropics.

In this study, we focus on the modifications of the PV resulting from heating. The effects of subgrid-scale processes ($\mathbf{F}$) are not examined. To determine the effects of heating on the PV, a heating function is specified as a combination of a leading convective heat source followed by a stratiform region heat source. The distribution of heating is represented by

$$\dot{\theta}(x,\theta,t) = \frac{Q_c d_c^{3/2}}{[(x-ct)^2 + d_c]^{3/2}} F_c(\theta)T(t) + \frac{Q_s d_s^{3/2}}{[(x+h-ct)^2 + d_s]^{3/2}} F_s(\theta)T(t), \qquad (7)$$

where subscript c (s) indicates the convective (stratiform) heating component, x and θ are the horizontal and vertical coordinates, respectively, t is time, c is the speed of the squall line, Q is the magnitude of the heating function, d controls the horizontal scale of the heating function, and h shifts the stratiform heat source horizontally relative to the convective heat source.

Terms F_c and F_s specify the normalized vertical distributions of the heating in the convective and stratiform regions, respectively, and vary from approximately -1 to 1 (Figs. 19a,b). We examine two cases in this section. For the first case, designated Case HS, F_c and F_s are sine functions as in HS91. This calculation shows that the model approximately reproduces the isentropic vorticity structure obtained in their calculations. For Case HS, the other parameters in the heating function (7) are $Q_c = 6$ K h^{-1}, $d_c = 1000$ km^2, $Q_s = 3$ K h^{-1}, $d_s = 3000$ km^2, and $h = 70$ km. These values produce a heating distribution (Fig. 20a) very similar to that of HS91 (see their Fig. 4). For the second case, designated Case BH, we base F_c and F_s on the convective and stratiform region heating profiles (eddy sensible heat flux convergence terms excluded) shown in Fig. 17. These heating profiles were normalized by dividing the heating rate at each level by the maximum value in the convective region and by the absolute value of the minimum value in the stratiform region (where the low-level cooling was stronger than the upper-level heating). The normalized heating profiles were then smoothed. For Case BH, $Q_c = 50$ K h^{-1}, $d_c = 80$ km^2, $Q_s = 7$ K h^{-1}, $d_s = 2000$ km^2, and $h = 70$ km. These magnitudes of Q_c and Q_s forced the area-averaged heating rates to match closely the magnitudes from the heat budget. The storm motion c in both cases was set to the observed value of 14 m s^{-1} (Rutledge et al. 1988; Biggerstaff and Houze 1991a).

The function $T(t)$ specifies the time variation of the heating. For Case HS, $T(t)$ is set to unity. For Case BH, it is assumed to have the form $T(t) = 1 - \exp(-t/t_0)$, where t_0 is the approximate timescale for the heat-

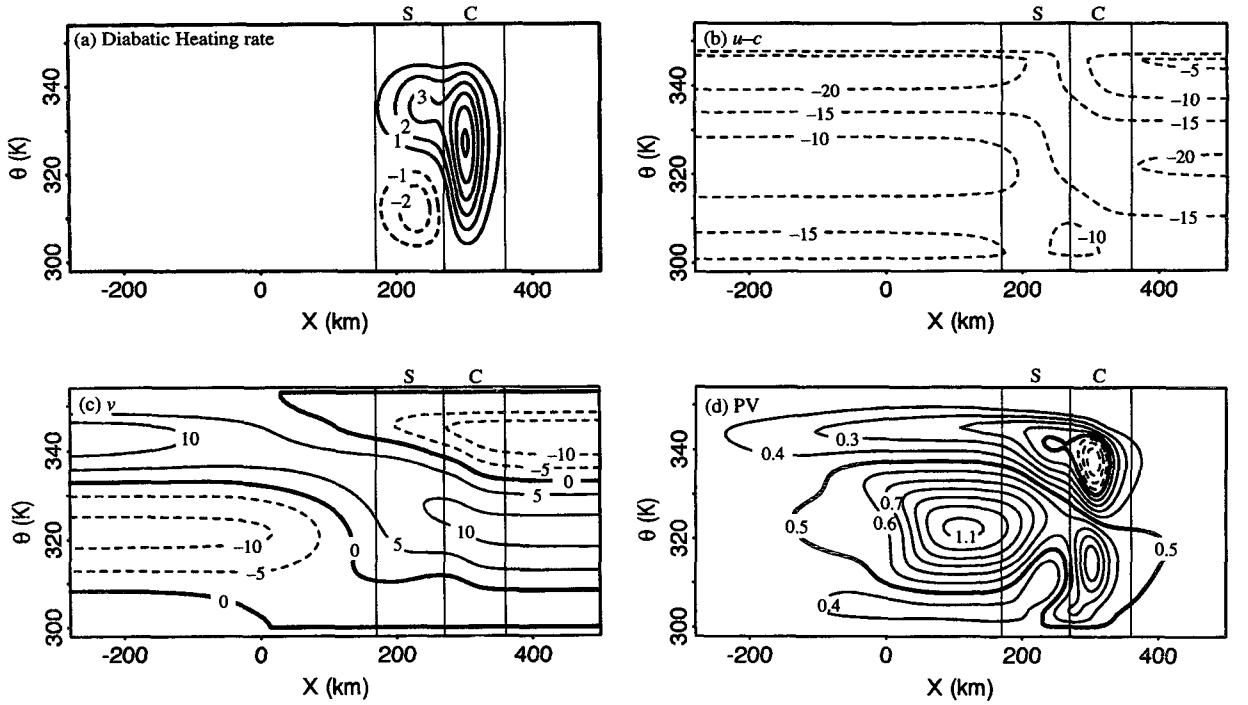

FIG. 20. (a) Heating function at 6 hours for Case HS. Contours drawn at 1 K h^{-1} intervals. (b) Across-line storm-relative wind component from (9), with contours drawn at 5 m s^{-1} intervals. (c) Along-line wind component contoured at 5 m s^{-1} intervals. (d) Potential vorticity contoured at 0.1 PVU intervals. Solid (dashed) contours indicate positive (negative) values. Bold lines indicate the 0 m s^{-1} contour in (c) and the 0 and 0.5 PVU contours in (d). Vertical lines indicate the approximate boundaries of the convective (C) and stratiform (S) heating regions.

ing to reach maturity. This time-dependent function is used to simulate the initial development of the convective line and the subsequent development of the stratiform region by gradually increasing the magnitudes of the heating rates. It does not simulate the evolution of the vertical variation of heating. The value of t_0 is set to 1 hour for the convective heat source and 3 hours for the stratiform heat source.

We restrict our computations to two dimensions ($x - \theta$). The x- (across-line) component of the wind, u, which is needed to compute the horizontal advection, is obtained by assuming that horizontal and temporal variations in σ are small enough that the two-dimensional mass continuity equation in isentropic coordinates can be approximated as

$$\frac{\partial u}{\partial x} = -\frac{1}{\sigma_0}\frac{\partial(\sigma_0\dot{\theta})}{\partial\theta}, \tag{8}$$

where σ_0 is a reference-state static stability, which is a function of potential temperature (height) only. The assumption that the horizontal and temporal variations in σ are small implies that the PV anomalies are dominated by perturbations in vorticity rather than stability. Davis and Weisman (1994) provide evidence that convectively generated PV anomalies are dominated by vorticity in mature convective systems. To simplify the calculations further, we assume σ_0 to be constant in the troposphere.[11] Consequently, (6) reduces to the vorticity equation in isentropic coordinates. For the heating function in (7), the mass continuity equation (8) implies that

$$u(x, \theta, t) = u_0(\theta, t) + \sigma_0^{-1} Q_c d_c^{3/2} \frac{x - ct}{d_c[(x - ct)^2 + d_c]^{1/2}} \frac{\partial(\sigma_0 F_c)}{\partial\theta} + \sigma_0^{-1} Q_s d_s^{3/2} \frac{x + h - ct}{d_s[(x + h - ct)^2 + d_s]^{1/2}} \frac{\partial(\sigma_0 F_s)}{\partial\theta}, \tag{9}$$

where u_0 is taken to be a mean geostrophic background wind component that depends only on θ and t. For Case HS, u_0 is set to zero to match the initial wind field of HS91. For Case BH, a time invariant u_0 is specified based on the across-line component of velocity taken from a sounding in the prestorm environment of the

[11] Calculations performed with σ_0 computed assuming a standard atmosphere (lapse rate = −6.5 K km^{-1}, surface temperature and pressure of 288 K and 1013 mb) showed no qualitative differences from calculations with σ_0 constant.

10–11 June storm (see Fig. 3b of Yang and Houze 1995a). This velocity profile was interpolated to isentropic coordinates and is shown in Fig. 19c.

The second term on the right of (6) requires the computation of the along-line (y) wind component, v, which is determined from the along-line component of the momentum equation

$$\frac{\partial v}{\partial t} + \frac{\partial (uv)}{\partial x} + \frac{\partial (\dot{\theta} v)}{\partial \theta} = -f(u - u_0), \quad (10)$$

where (8) has been used to express the left side of (10) in flux form and u_0 is assumed to be geostrophically balanced with a background along-line pressure gradient. Because of the assumption of constant σ_0, the isentropic vorticity, expressed in PV units, is obtained from $(\partial v/\partial x + f)/\sigma_0$. Although it is not strictly potential vorticity, we will denote the isentropic vorticity by PV hereafter.

Equation (10) was integrated on a grid 1000 km in length and 54 K in height, with horizontal and vertical grid spacing of 4 km and 1 K, respectively. The heating (7) was applied to the lower 47 isentropic levels. A third-order Adams–Bashforth scheme was used for time differencing. Spatial differencing was calculated following Haltiner and Williams (1980, p. 178). The initial along-line wind component was set to zero in Case HS. In Case BH, in order to specify initial conditions more representative of the 10–11 June squall line, it was prescribed by a surface wind of -5 m s^{-1} and a background vertical wind shear of 25 m s^{-1}/47 K. The Coriolis parameter f was set to 8.6×10^{-5} s^{-1} (latitude = 36°) and σ_0 to 175 kg m^{-2} K^{-1}, which yields an initial PV of 0.5 PVU (1 PV Unit = 10^{-6} m^2 s^{-1} K kg^{-1}).

Figure 20 shows cross sections of $\dot{\theta}$, $u - c$, v, and PV at 6 hours for Case HS. The across-line storm-relative flow ($u - c$, Fig. 20b) is entirely front to rear and is characterized by upper-level divergence and midlevel convergence. The along-line wind component (Fig. 20c) indicates a midlevel cyclonic circulation and upper- and lower-level anticyclonic circulations. The associated PV field (Fig. 20d) is characterized by a midlevel cyclonic PV anomaly and upper- and lower-level anticyclonic PV anomalies within and to the rear of the stratiform precipitation region. This PV pattern is nearly identical to that in HS91. In the convective region, however, a low-level cyclonic PV anomaly and an upper-level anticyclonic PV anomaly (with negative PV) are present. These PV features were not produced in HS91. The difference in PV structure results from the fact that HS91 defined their heat source in geostrophic, rather than physical, coordinates. This procedure is equivalent to neglecting the tilting terms in the vorticity equation [i.e., terms involving the horizontal vorticity components in the physical-coordinate version of their PV equation; see (2.7) of Schubert et al. (1989)]. The along-line wind component (Fig. 20c) indicates that the heat source resided in a region of positive (negative) vertical wind shear at lower (upper) levels. The convective-region PV anomalies were produced by the tilting of this horizontal vorticity.

Figure 21 shows cross sections of the $\dot{\theta}$, $u - c$, and v fields at 6 hours for Case BH. Note that the values of the contours for the heating function and v in Fig. 21 differ from those in Fig. 20 because of the much stronger heating rates in Case BH. The $u - c$ field (Fig. 21b) is characterized by strong divergent outflow at the top of the convective region and rear inflow just above the melting level (~315 K) in the stratiform region. The rear inflow occurs just above the melting level be-

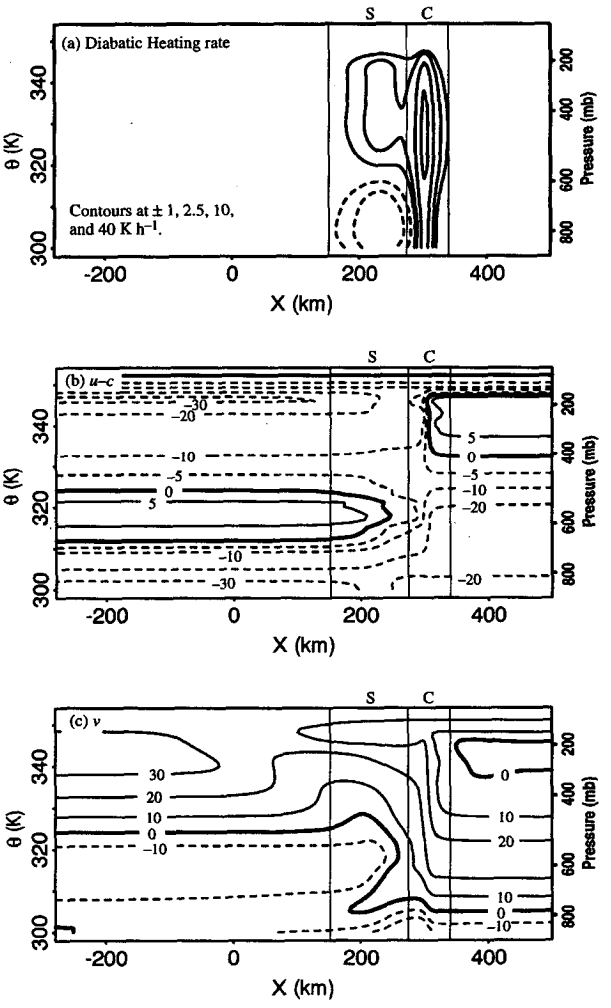

FIG. 21. (a) Heating function at 6 hours for Case BH. (b) Across-line storm-relative wind component. Contours are drawn at 10 m s^{-1} intervals, with additional contours drawn at ±5 m s^{-1}. (c) Along-line wind component contoured at 10 m s^{-1} intervals. Solid (dashed) contours indicate positive (negative) values. Bold lines indicate the 0 m s^{-1} contour. Vertical lines indicate the approximate boundaries of the convective (C) and stratiform (S) heating regions. Approximate pressure levels corresponding to the isentropic levels are indicated along the right vertical axis.

cause of the convergence implied by (8) above the peak cooling by melting. Interestingly, when the cooling and heating associated with melting and freezing are neglected in F_c and F_s, the strength of the rear inflow is substantially reduced by approximately 6 m s^{-1}. Yang and Houze (1995b) found a 25% (~2 m s^{-1}) reduction of rear-inflow strength when melting was excluded in their simulation. Such sensitivity to melting thus emphasizes the importance of ice microphysical processes to circulations in MCSs and to the realistic simulation of MCSs in models. A front to rear current extends from low to midlevels ahead of the convective region to upper levels within and rearward of the stratiform region. Strong front to rear flow also occurs at low levels where it exits the stratiform region. Thus, the prescribed across-line flow qualitatively resembles observed flow characteristics of the 10–11 June storm (Rutledge et al. 1988; Biggerstaff and Houze 1993). The v field (Fig. 21c) shows strong southerly (positive values) at midlevels ahead of the convective region. The southerly flow rises sharply within the convective region. A strong southerly jet is located at upper levels to the rear of the stratiform heating region. Northerly flow is generally located at low to midlevels within and to the rear of the heating region.

The evolution of the PV field for Case BH is depicted in Fig. 22. The contour values are greater than in Fig. 20d since the stronger heating yielded much larger PV anomalies. After 2 hours (Fig. 22a), a deep column of high-PV air was located within the convective region with maximum values in excess of 2 PVU near 320 K. A region of negative PV was located at upper levels within the stratiform region and the rear portion of the convective region (i.e., within the transition zone). By 4 hours (Fig. 22b), this negative-PV region drifted rearward and new regions of negative PV formed in the upper and forward portion of the convective region, similar to Case HS (Fig. 20d), and at low levels in the stratiform region. According to (6), these regions of negative PV were generated by the apparent momentum source since the first term on the right of (6) cannot change the sign of the PV. The low- to midlevel cyclonic PV in the convective region increased in magnitude to 4 PVU near 320 K. A secondary PV maximum began to form in the stratiform region between 310 and 320 K. At 6 hours (Fig. 22c), the PV anomalies in the heating regions intensified further. The secondary PV maximum in the stratiform region was well defined. The region of negative PV that had originally formed immediately to the rear of the convective line (Fig. 22a) extended from the rear of the stratiform region into the wake region behind the squall line by 6 hours.

Biggerstaff and Houze (1991b) examined the vorticity structure of the 10–11 June squall line. A vertical cross section, oriented normal to the line, of the vertical component of absolute vorticity was computed from their data fields and is shown in Fig. 23. It shows that

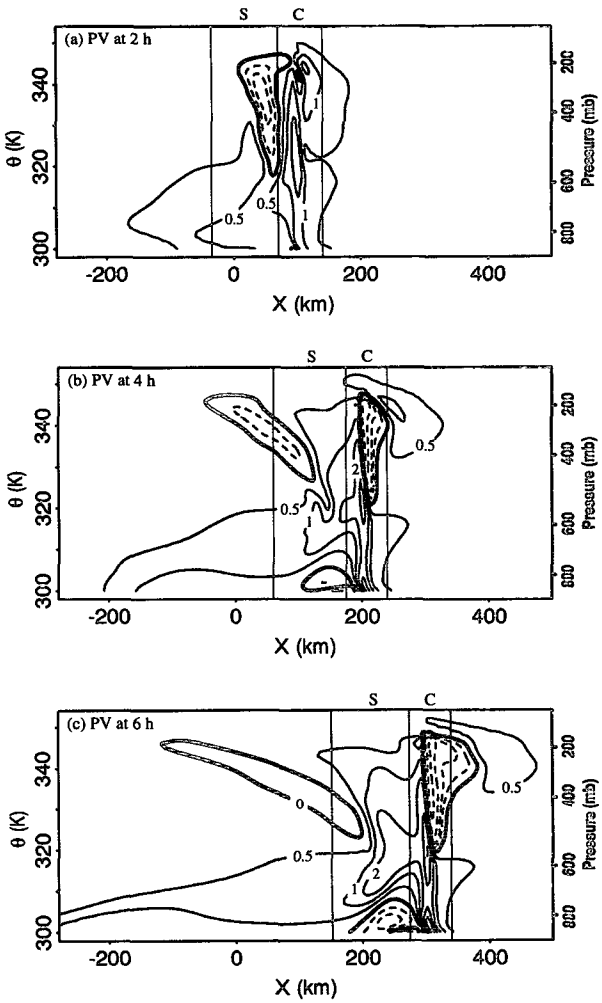

FIG. 22. Potential vorticity for Case BH at (a) 2, (b) 4, and (c) 6 hours. PV contours are drawn at ±0.5, 1, 2, 4, and 6 PVU. Positive (negative) values are indicated by the solid (dashed) lines. The 0 PVU contour is drawn as the bold solid line. Vertical lines indicate the approximate boundaries of the convective (C) and stratiform (S) heating regions. Approximate pressure levels corresponding to the isentropic levels are indicated along the right vertical axis.

a deep column of strong cyclonic vorticity was present in the observations of the convective region. The stratiform and transition zone regions of the squall line were characterized by negative absolute vorticity (and hence, negative PV) along some portions of the squall line at mid to upper levels. Biggerstaff and Houze (1991b) showed that this negative vorticity was produced by tilting of horizontal vorticity by the convective region vertical motions. Figure 23 shows that negative absolute vorticity was also present at mid to upper levels immediately ahead of the column of large cyclonic vorticity. The PV model (Fig. 22) reproduced the qualitative features of the observed vorticity distribution in Fig. 23.

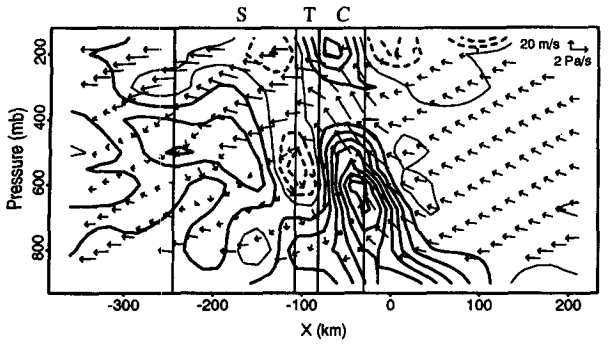

FIG. 23. Contours of absolute vorticity at intervals of 1.0×10^{-4} s^{-1}. Positive (negative) values are indicated by the solid (dashed) lines. The 0 PVU contour is drawn as the thin solid line. Arrows indicate storm-relative circulation vectors. Vertical lines indicate approximate boundaries of the convective (C), transition (T), and stratiform (S) regions. The data are obtained from the dual-Doppler and rawinsonde composite analysis of Biggerstaff and Houze (1991a,b). The cross section is located at $Y = 60$ km in their coordinate system [see Fig. 6 of Biggerstaff and Houze (1991a)].

Zhang et al. (1989) and Zhang (1992) have also reproduced some of these vorticity features in a mesoscale model simulation of the squall line. Tollerud and Esbensen (1983) and Mapes and Houze (1992) have found regions of negative absolute vorticity at upper levels associated with tropical mesoscale convective systems and have suggested that the negative vorticity resulted from vertical momentum transports by the convective systems. These results, along with those of Biggerstaff and Houze (1991b), are consistent with our results.

The generation of negative potential vorticity by the squall line can be associated with significant feedbacks to the larger-scale flow at upper levels. The negative PV (absolute vorticity) implies the possibility of symmetric (inertial) instability. Zhang and Cho (1992) and Seman (1994) have suggested that such instability would favor intensification of the upper-level outflow within and to the rear of squall lines. Strong upper-level jet maxima have been observed northwestward to northward of mesoscale convective systems (Ninomiya 1971a,b; Fritsch and Maddox 1981; Keyser and Johnson 1984). Keyser and Johnson (1984) proposed that such jet maxima can result from anticyclonic inertial turning of the upper-level outflow. Braun (1995), in a simulation of the 10–11 June squall line using the Penn State–NCAR nonhydrostatic mesoscale model (MM5),[12] found that the 10–11 June squall line enhanced the upper-level jet stream by up to 20 m s^{-1} in the sector located northwest to northeast of the squall line. The enhancement of the jet stream occurred in association with the generation by the squall line of a tongue of negative PV and its subsequent advection downstream by the larger-scale flow. The jet axis lay along the northwestern and northern edge of this negative PV tongue. This relationship between an enhanced upper-level jet and a zone of negative PV (originating from squall line dynamics) was reproduced by the PV model (Figs. 21c and 22c). The region of negative PV at upper levels to the rear of the stratiform region marked the strong anticyclonic shear zone on the eastern (positive x) side of the upper-level jet in the along-line flow.

[12] The initialization procedure follows that described in Zhang et al. (1989). The model setup is similar to Zhang et al. (1989) except that it is nonhydrostatic, no correction is applied to the precipitation fall speeds, and there are 28 vertical levels compared to 19.

8. Conclusions

Water and heat budgets have been derived for the 10–11 June 1985 squall line for its early and mature stages. Data from single and dual Doppler radars and rawinsonde have been combined with output from thermodynamic and microphysical retrieval algorithms (one- and two-dimensional) and with a radiative transfer model to differentiate the processes contributing to the total heating within the convective, stratiform, and anvil areas of the squall line. Since vertical velocity information from the radars provided the basis for these calculations, the contributions of the convective and stratiform precipitation regions to the total heating were more precisely delineated than in the rawinsonde-based study of Gallus and Johnson (1991, GJ).

Water budget calculations indicate that during the early stages of the squall line the total source of condensate in the stratiform region was dominated by the horizontal transport of condensate from the convective region (87%). As the squall line matured, the convective line began to weaken and the mesoscale ascent strengthened. As a result, during the mature stage, the contribution from condensation and deposition within the mesoscale updraft to the total source of condensate in the stratiform region had increased from 13% to 35%. This value is smaller than the value of 54% found in the rawinsonde-based study of GJ.

In the heat budget, condensation dominated the convective-region total-heating profile except below the 0°C level where strong cooling from melting, evaporation, and the convergence of the eddy heat flux acted to cancel a significant portion of the condensation heating. The total convective heating profile exhibited relatively uniform net heating below the melting level and then increased rapidly within a 1-km deep layer above the melting level as the cooling by melting transitioned to heating by freezing. Longwave cooling at cloud top was negligible in the convective region.

In the stratiform region during the early stage, the heating profile was characterized by strong cooling below and weak heating above 6 km. By the mature stage of the squall line, cooling in the lower troposphere and heating in the upper troposphere had nearly doubled,

with the transition from cooling to heating occurring at the 0°C level near 4 km. A breakdown of the heating profile into its separate components during the mature stage indicated that the cooling in the lower troposphere was dominated by evaporation, although just below the 0°C level evaporation and melting produced cooling rates of similar magnitude. Radiative cooling near cloud top was small compared to latent heating at lower levels. While longwave radiative cooling near cloud top in the precipitating regions appeared to be of minor importance, such cooling in the nonprecipitating anvil region was important because of the large area covered by the anvil cloud.

The heating profiles within the convective, stratiform, and anvil regions yielded a total heating profile during the early stage characterized by virtually no net heating in the lower troposphere (below 4.5 km) where the stratiform region cooling canceled the convective heating and by strong heating in the upper troposphere where stratiform region heating augmented the convective heating. During the mature stage, the increased cooling in the lower troposphere led to net cooling in the lowest 3 km, while in the upper troposphere, stronger stratiform region heating combined with weaker convective heating maintained the strong heating in the upper troposphere. A comparison of the radar-derived heating rates to the rawinsonde-based calculations of GJ confirm GJ's supposition that a significant fraction of their early stage (0300 UTC) stratiform-region heating was actually associated with convective vertical motions that were aliased into the stratiform region because of the coarse horizontal resolution of their dataset.

We investigated the effect of the squall system on the large-scale environmental circulation by using the heating distribution derived from observations as input to a simple two-dimensional calculation of the potential vorticity field in and around the storm. When a heat source appropriate to a leading line–trailing stratiform squall line was assigned relatively weak heating rates (Case HS), the model produced PV anomalies very similar to those of HS91, that is, a midlevel positive PV anomaly and lower- and upper-level negative PV anomalies within and to the rear of the stratiform region. However, the circulation was too weak and no rear inflow occurred.

When the vertical distribution and magnitude of the heating were based on the observed heat budget results (Case BH), the implied circulation was much more realistic. The air motions were stronger and included a rear-inflow jet, which was absent in Case HS. The heating produced a deep column of high PV air coincident with the convective region and produced three regions of negative potential vorticity: 1) in the upper and forward portion of the convective region, 2) at upper levels within and to the rear of the stratiform region, and 3) at low levels in the stratiform region. Similar regions of negative PV were observed in the 10–11 June storm. The upper-level negative PV suggests that symmetric or inertial instability might favor intensification of the upper-level line-normal outflow within and to the rear of the stratiform region. Anticyclonic inertial turning of this outflow contributes to the formation of a strong upper-level jet in the line-parallel flow to the rear of the squall line.

Further research is required to document the upscale feedbacks of the squall line, to diagnose their contribution to low-level cyclogenesis and upper-level jet-stream enhancement, and to understand their dependence on storm organization and on microphysical processes. Work is in progress to document the three-dimensional structure and evolution of the PV fields associated with the 10–11 June squall line by means of a mesoscale model simulation for this case and to relate the PV fields to the observed evolution of the larger-scale flow.

Acknowledgments. We would like to thank Drs. Takmeng Wong, Paul Stackhouse, and Graeme Stephens for the use of their radiative transfer model, Drs. William Gallus and Richard Johnson for their heat budget profiles, Dr. Michael Biggerstaff for the dual-Doppler and composite analysis data, and Dr. Ming-Jen Yang for the cloud model fields. We thank Drs. Christopher Bretherton, Dale Durran, and Margaret LeMone and the reviewers for their helpful comments. G. C. Gudmundson edited the manuscript and Kay Dewar helped draft the figures. This research was sponsored by National Science Foundation Grant ATM-9409988.

REFERENCES

Augustine, J. A., and E. J. Zipser, 1987: The use of wind profilers in a mesoscale experiment. *Bull. Amer. Meteor. Soc.*, **68,** 4–17.

Bartels, D. L., and R. A. Maddox, 1991: Midlevel cyclonic vortices generated by mesoscale convective systems. *Mon. Wea. Rev.*, **119,** 104–118.

Biggerstaff, M. I., and R. A. Houze, Jr., 1991a: Kinematic and precipitation structure of the 10–11 June 1985 squall line. *Mon. Wea. Rev.*, **119,** 3034–3065.

——, and ——, 1991b: Midlevel vorticity structure of the 10–11 June 1985 squall line. *Mon. Wea. Rev.*, **119,** 3066–3079.

——, and ——, 1993: Kinematics and microphysics of the transition zone of the 10–11 June 1985 squall-line. *J. Atmos. Sci.*, **50,** 3091–3110.

Bosart, L. F., and F. Sanders, 1981: The Johnstown flood of 1977: A long-lived convective storm. *J. Atmos. Sci.*, **38,** 1616–1642.

Braun, S. A., 1995: Multiscale process interactions associated with a midlatitude squall line. Ph.D. thesis, University of Washington, 194 pp.

——, and R. A. Houze Jr., 1994: The transition zone and secondary maximum of radar reflectivity behind a midlatitude squall line: Results retrieved from Doppler radar data. *J. Atmos. Sci.*, **51,** 2733–2755.

——, and ——, 1995a: Diagnosis of hydrometeor profiles from area-mean vertical velocity data. *Quart. J. Roy. Meteor. Soc.*, **121,** 23–53.

——, and ——, 1995b: Melting and freezing in a mesoscale convective system. *Quart. J. Roy Meteor. Soc.*, **121,** 55–77.

Chen, S. S., and W. M. Frank, 1993: A numerical study of the genesis of extratropical convective mesovortices. Part I: Evolution and dynamics. *J. Atmos. Sci.*, **50,** 2401–2426.

Chong, M., and D. Hauser, 1990: A tropical squall line observed during the COPT 81 experiment in West Africa. Part III: Heat and moisture budgets. *Mon. Wea. Rev.*, **118,** 1696–1706.

Cunning, J. B., 1986: The Oklahoma–Kansas Preliminary Regional Experiment for STORM-Central. *Bull. Amer. Meteor. Soc.*, **67,** 1478–1486.

Davis, C. A., and M. L. Weisman, 1994: Balanced dynamics of mesoscale vortices produced in simulated convective systems. *J. Atmos. Sci.*, **51,** 2005–2030.

——, M. T. Stoelinga, and Y.-H. Kuo, 1993: The integrated effect of condensation in numerical simulations of extratropical cyclogenesis. *Mon. Wea. Rev.*, **121,** 2309–2330.

Fritsch, J. M., and R. A. Maddox, 1981: Convectively driven mesoscale weather systems aloft. Part I: Observations. *J. Appl. Meteor.*, **20,** 20–26.

——, J. D. Murphy, and J. S. Kain, 1994: Warm core mesovortex amplification over land. *J. Atmos. Sci.*, **51,** 1780–1807.

Gallus, W. A., Jr., 1994: The dynamics of circulations within the stratiform regions of squall lines. Preprints, *Sixth Conf. on Mesoscale Processes,* Portland, Amer. Meteor. Soc., 611–614.

——, and R. H. Johnson, 1991: Heat and moisture budgets of an intense midlatitude squall line. *J. Atmos. Sci.*, **48,** 122–146.

Haltiner, G. J., and R. T. Williams, 1980: *Numerical Prediction and Dynamic Meteorology,* 2d ed. John Wiley and Sons, 477 pp.

Haynes, P. H., and M. E. McIntyre, 1987: On the evolution of vorticity and potential vorticity in the presence of diabatic heating and frictional or other forces. *J. Atmos. Sci.*, **44,** 828–840.

Hertenstein, R. F. A., and W. H. Schubert, 1991: Potential vorticity anomalies associated with squall lines. *Mon. Wea. Rev.*, **119,** 1663–1672.

Holton, J. R., 1992: *An Introduction to Dynamic Meteorology,* 3d ed. Academic Press, 511 pp.

Hoskins, B. J., M. E. McIntyre, and A. W. Robertson, 1985: On the use and significance of isentropic potential vorticity maps. *Quart. J. Roy. Meteor. Soc.*, **111,** 877–946.

Houze, R. A., Jr., 1982: Cloud clusters and large-scale vertical motions in the Tropics. *J. Meteor. Soc. Japan,* **60,** 396–410.

——, B. F. Smull, and P. Dodge, 1990: Mesoscale organization of springtime rainstorms in Oklahoma. *Mon. Wea. Rev.*, **118,** 613–654.

Johnson, R. H., and P. J. Hamilton, 1988: The relationship of surface pressure features to the precipitation and airflow structure of an intense midlatitude squall line. *Mon. Wea. Rev.*, **116,** 1444–1472.

——, and D. L. Bartels, 1992: Circulations associated with a mature to decaying midlatitude mesoscale convective system. Part II: Upper-level features. *Mon. Wea. Rev.*, **120,** 1301–1320.

Keyser, D. A., and D. R. Johnson, 1984: Effects of diabatic heating on the ageostrophic circulation of an upper-tropospheric jet streak. *Mon. Wea. Rev.*, **112,** 1709–1724.

Leary, C. A., and R. A. Houze, Jr., 1979: Melting and evaporation of hydrometeors in precipitation from anvil clouds of deep tropical convection. *J. Atmos. Sci.*, **36,** 669–679.

——, and ——, 1980: The contribution of mesoscale motions to the mass and heat fluxes of an intense tropical convective system. *J. Atmos. Sci.*, **37,** 784–796.

Lilly, D. K., 1988: Cirrus outflow dynamics. *J. Atmos. Sci.*, **45,** 1594–1605.

Lin, Y.-L., R. D. Farley, and H. D. Orville, 1983: Bulk parameterization of the snow field in a cloud model. *J. Climate Appl. Meteor.*, **22,** 1065–1092.

Mapes, B., and R. A. Houze, Jr., 1992: An integrated view of the 1987 Australian monsoon and its mesoscale convective systems. Part I: Horizontal structure. *Quart. J. Roy. Meteor. Soc.*, **118,** 927–963.

——, and ——, 1993: An integrated view of the 1987 Australian monsoon and its mesoscale convective systems. Part II: Vertical structure. *Quart. J. Roy. Meteor. Soc.*, **119,** 733–753.

——, and ——, 1995: Diabatic divergence profiles in western Pacific mesoscale convective systems. *J. Atmos. Sci.*, **52,** 1807–1828.

Ninomiya, K., 1971a: Dynamical analysis of outflow from tornado-producing thunderstorms as revealed by ATS III pictures. *J. Appl. Meteor.*, **10,** 275–294.

——, 1971b: Mesoscale modification of synoptic situations from thunderstorm development as revealed by ATS III and aerological data. *J. Appl. Meteor.*, **10,** 1103–1121.

Rutledge, S. A., R. A. Houze, Jr., M. I. Biggerstaff, and T. Matejka, 1988: The Oklahoma–Kansas mesoscale convective system of 10–11 June 1985: Precipitation structure and single-Doppler radar analysis. *Mon. Wea. Rev.*, **116,** 1409–1430.

Schubert, W. H., S. R. Fulton, and R. F. A. Hertenstein, 1989: Balanced atmospheric response to squall lines. *J. Atmos. Sci.*, **46,** 2478–2483.

Seman, C. J., 1994: A numerical study of nonlinear nonhydrostatic conditional symmetric instability in a convectively unstable atmosphere. *J. Atmos. Sci.*, **51,** 1352–1371.

Smull, B. F., and R. A. Houze, Jr., 1987: Dual-Doppler radar analysis of a midlatitude squall line with a trailing region of stratiform rain. *J. Atmos. Sci.*, **44,** 2128–2148.

Srivastava, R. C., T. J. Matejka, and T. J. Lorello, 1986: Doppler-radar study of the trailing-anvil region associated with a squall line. *J. Atmos. Sci.*, **43,** 356–377.

Stackhouse, P. W., Jr., and G. L. Stephens, 1991: A theoretical and observational study of the radiative properties of cirrus: Results from FIRE 1986. *J. Atmos. Sci.*, **48,** 2044–2059.

Stensrud, D. J., R. A. Maddox, and C. L. Ziegler, 1991: A sublimation-initiated mesoscale downdraft and its relation to the wind field below a precipitating anvil cloud. *Mon. Wea. Rev.*, **119,** 2124–2139.

Szeto, K. K., R. E. Stewart, and C. A. Lin, 1988: Mesoscale circulations forced by melting snow. Part II: Application to meteorological features. *J. Atmos. Sci.*, **45,** 1642–1650.

Tao, W.-K., J. Simpson, C.-H. Sui, B. Ferrier, S. Lang, J. Scala, M.-D. Chou, and K. Pickering, 1993: Heating, moisture, and water budgets of tropical and midlatitude squall lines: Comparisons and sensitivity to longwave radiation. *J. Atmos. Sci.*, **50,** 673–690.

Tollerud, E. I., and S. K. Esbensen, 1983: An observational study of the upper-tropospheric vorticity fields in GATE cloud clusters. *Mon. Wea. Rev.*, **111,** 2161–2175.

Wong, T., G. L. Stephens, P. W. Stackhouse, Jr., and F. P. J. Valero, 1993: The radiative budgets of a tropical mesoscale convective system during EMEX-STEP-AMEX Experiment. Part II: Model results. *J. Geophys. Res.*, **98**(D5), 8683–8693.

Yang, M.-J., and R. A. Houze Jr., 1995a: Multicell squall line structure as a manifestation of vertically trapped gravity waves. *Mon. Wea. Rev.*, **123,** 641–661.

——, and ——, 1995b: Sensitivity of squall-line rear inflow to ice microphysics and environmental humidity. *Mon. Wea. Rev.*, **123,** 3175–3193.

Yuter, S., and R. A. Houze Jr., 1995: Three-dimensional kinematic and microphysical evolution of Florida cumulonimbus, Part II: Frequency distributions of vertical velocity, reflectivity, and differential reflectivity. *Mon. Wea. Rev.*, **123,** 1941–1963.

Zhang, D.-L., 1992: Formation of a cooling-induced mesovortex in the trailing stratiform region of a midlatitude squall line. *Mon. Wea. Rev.*, **120,** 2763–2785.

——, and J. M. Fritsch, 1987: Numerical simulation of the meso-β scale structure and evolution of the 1977 Johnstown flood. Part II: Inertially stable warm-core vortex and the mesoscale convective complex. *J. Atmos. Sci.*, **44,** 2593–2612.

——, and ——, 1988: A numerical investigation of a convectively generated, inertially stable, extratropical warm-core mesovortex over land. Part I: Structure and evolution. *Mon. Wea. Rev.*, **116,** 2660–2687.

——, and H.-R. Cho, 1992: The development of negative moist potential vorticity in the stratiform region of a simulated squall line. *Mon. Wea. Rev.*, **120,** 1322–1341.

——, and R. Harvey, 1995: Enhancement of extratropical cyclogenesis by a mesoscale convective system. *J. Atmos. Sci.*, **52,** 1107–1127.

——, K. Gao, and D. B. Parsons, 1989: Numerical simulation of an intense squall line during 10–11 June 1985 PRE-STORM. Part I: Model verification. *Mon. Wea. Rev.*, **117,** 960–994.